A climatology of microbarom detections at the Kerguelen Islands
Unravelling the ambient noise wavefield

Den Ouden, Olivier F.C.; Assink, Jelle D.; Smets, Pieter S.M.; Evers, Läslo G.

DOI
10.1093/gji/ggab535

Publication date
2022

Document Version
Final published version

Published in
Geophysical Journal International

Citation (APA)
Den Ouden, O. F. C., Assink, J. D., Smets, P. S. M., & Evers, L. G. (2022). A climatology of microbarom detections at the Kerguelen Islands: Unravelling the ambient noise wavefield. *Geophysical Journal International*, *229*(3), 1646-1664. https://doi.org/10.1093/gji/ggab535

Geophysical Journal International

Geophys. J. Int. (2022) **229,** 1646–1664
Advance Access publication 2022 January 04
GJI Seismology

https://doi.org/10.1093/gji/ggab535

A climatology of microbarom detections at the Kerguelen Islands: unravelling the ambient noise wavefield

Olivier F.C. den Ouden [1,2] Jelle D. Assink,[1] Pieter S.M. Smets [2] and Läslo G. Evers [1,2]

[1]*R&D Department of Seismology and Acoustics, Royal Netherlands Meteorological Institute, De Bilt, the Netherlands. E-mail: olivier.den.ouden@knmi.nl*
[2]*Department of Geoscience and Engineering, Delft University of Technology, Delft, the Netherlands*

Accepted 2022 0. Received 2021 December 30; in original form 2021 October 1

SUMMARY

The ambient infrasonic noise field is complex due to the interference of spatially distributed infrasound sources. Microbaroms are one of the most dominant omnipresent infrasonic sources within this wavefield. These microbaroms are generated by nonlinear ocean surface wave interactions, and have a characteristic and continuous signature within the infrasound spectrum. Under noisy conditions, microbaroms can mask infrasonic signals of interest, such as infrasound from volcanoes or explosions, which limits detection and identification of such sources. This study performs an infrasonic climatology for infrasound array I23FR, using five years of data between 2015–2020. The array is located on the Kerguelen Islands, within the Southern Ocean, and is part of the International Monitoring System for the verification of the Comprehensive Nuclear-Test-Ban Treaty. The climatology analysis addresses the expected ambient noise levels, propagation paths and potential sources within the vicinity of an infrasound sensor. Time- and frequency-domain beamforming methods have been applied to analyse the infrasonic wavefield from the I23FR observations. A recently introduced method is applied to compute so-called soundscapes, to be compared with beamform results. Although the comparison indicates a disagreement in amplitude, there is a good agreement in directionality and frequency between both.

Key words: Indian Ocean; Infrasound;; Time-series analysis.

1 INTRODUCTION

The atmosphere, earth and ocean are globally monitored by the International Monitoring System (IMS) for the verification of the Comprehensive Nuclear-Test-Ban Treaty (CTBT). The infrasound component of the IMS monitors the infrasonic wavefield. IMS microbarometer arrays provide real-time infrasound recordings from around the world. Therefore, the IMS has played a central role in the characterization of the global low-frequency wavefield (i.e. frequencies lower than 20 Hz) and the localization of sound sources (Campus & Christie 2010; Marty 2019).

Infrasound station I23FR is one of the IMS microbarometer arrays and provides real-time monitoring. The array is located at the Kerguelen Islands, which is part of the French Sub-antarctic and Antarctic lands (Fig. 1). The microbarometer array is located on the east side of the main island and consists of 15 microbarometers, which is the largest number of elements within the IMS infrasound network (Marty 2019). Although I23FR continuously monitors the infrasonic wavefield on the boundary of the Indian and Southern Ocean, the array is often excluded from scientific studies due to the environmental conditions (Brown *et al.* 2014). The islands experience strong surface winds and severe weather conditions. Local noise conditions (e.g. wind turbulence) may mask infrasonic signals of interest (Raspet *et al.* 2019). Nonetheless, the IMS infrasound station density at mid-latitudes is lower for the Southern Hemisphere compared to the Northern Hemisphere. Hence, understanding the infrasonic wavefield surrounding I23FR will be important if there was ever a suspected test within the Southern Hemisphere.

I23FR is located on the Kerguelen Plateau near the Indian and Southern Ocean intersection, where various ocean currents meet. Deep oceanic ambient noise is globally the most omnipresent infrasound source. The driving force of the ambient atmospheric noise (i.e. microbaroms) is the sea state, which describes the energy of the ocean travelling surface waves. Nonlinear interaction of counter travelling ocean surface waves results in standing ocean waves, causing the radiation of acoustic energy and resonance within the water column (Longuet-Higgins 1950; Hasselmann 1963). At the interfaces of the water column, acoustic energy is radiated into the atmosphere resulting in microbaroms (Brekovskikh 1973). Microbaroms typically peak around 0.2 Hz, with a characteristic amplitude range of 55–110 dB with respect to 20 micro-pascals (Campus & Christie 2010). Earlier studies have shown that the microbarom signal can be a dominant background noise signal (Donn & Rind 1972) that can obscure signals of interest, for example volcanic eruptions (McKee *et al.* 2021). Microbarom signals can, therefore, potentially mask other infrasonic signals of interest. Characterizing

microbaroms is essential for the understanding of the infrasonic wavefield. Knowledge regarding frequency, amplitude and propagation of the microbaroms could help assess the microbarom source contributions to the infrasonic wavefield, which adds to a better understanding of the IMS's verification capability and infrasound as a remote sensing technique for the upper atmosphere (Donn & Rind 1972; Smets 2018).

This study performs an infrasonic climatology for infrasound array I23FR, using five years of data between 2015–2020. Within this climatology study, various tools are combined. The analysis addresses the expected noise levels, propagation paths, and potential sources within the vicinity of the infrasound array. The analysis gives insights into the performance of an infrasound array and the ability to resolve infrasonic sources. Previous studies have introduced and applied various methods to unravel and characterize the wavefield into individual components (Landes *et al.* 2012; Matoza *et al.* 2013; De Carlo *et al.* 2020).

The climatology study outlined within this paper is based on *in-situ* observations of I23FR and model data. Therefore the analysis allows for a comparison and validation of the model, which determines the reliability as a measure for the infrasonic wavefield. The *in-situ* observations depend on the array layout and system response of the array elements. Moreover, meteorological phenomena may influence the detection capability of an infrasound array. Meteorological data are used to determine the local noise conditions at the ground and the propagation conditions of infrasound with altitude. These observations highlight expected noise conditions and seasonality of the infrasound conditions at an array.

The *in-situ* infrasound observations include microbarometer array recordings to evaluate the noise levels and apply data processing techniques for separating the wavefield into a coherent and incoherent part. The model analysis covers omnidirectional infrasoundscapes, reconstructed from the perspective of the array (den Ouden *et al.* 2021). Such soundscapes provide the infrasonic sound levels in the vicinity of the array from a theoretical and model perspective. A comparison is performed to indicate the agreement between *in-situ* observations and model data.

The article is organized as follows. Section 2 discusses the array layout, array responses and the system response. The meteorological conditions influencing the local noise conditions and propagation conditions are reviewed in Section 3. Within Section 4, the infrasound observations are analysed by applying data processing techniques. Section 5 addresses the reconstruction of infrasonic soundscapes and the interpretation of these. The comparison between the soundscapes and the observations is described in Section 6. The outcome of this climatology study is summarized and discussed in the final section.

2 MICROBAROMETER ARRAY I23FR, KERGUELEN ISLANDS

Microbarometer arrays are used to study the infrasonic wavefield. The use of arrays allows for enhanced detection of signals in the presence of incoherent noise, as the signal-to-noise ratio (SNR) is improved by summation across the array elements. In addition, array processing enables to resolve the direction, apparent velocity and frequency content of the impinging wave front. Localization and characterization of the source depend on the source–receiver distance. Nearby sources can be distinguished as spherical wave fronts and localized by single arrays (Szuberla *et al.* 2009; Stettner 2018). Distant sources, however, can be characterized by planar waves. Localization of distant sources is possible by combining various array detections through the process of cross-bearing the resolved backazimuths (Evers 2008; den Ouden *et al.* 2020).

The I23FR microbarometer array is divided into five identical triplets of ∼100 m aperture (Fig. 1c). The inter distance between the triplets is ∼500 m, while the total aperture is ∼1750 m. The closely spaced triplet elements enhance the detection and parameter estimation at higher frequencies which may be less coherent over the entire array (Campus & Christie 2010). The lower frequencies of the wavefield are resolved by combining elements of the various triplets.

Atmospheric noise limits the ability to detect signals of interest due to the influence of near-surface wind close to the microbarometer. Therefore, each microbarometer array has a different detection threshold for monitoring, which varies significantly due to those local wind conditions. A vital consequence of this is that the background noise between arrays and array elements is different. This has implications for infrasound array processing (Walker & Hedlin 2010).

The array elements at I23FR consist of (1) MB2005 microbarometers and a (2) wind noise reduction system (Fig. 2a) to establish theoretically similar noise conditions. The absolute microbarometers provide a flat-to-pressure response across (and beyond) the 0.02–4 Hz passband required by the IMS specifications (Figs 2b and c, Supporting Information S1). The WNRS is a 108-inlet, 36 m diameter, hexagonal pipe rosette (see Table 1 for specifications). Moreover, all inlets are covered with gravel to reduce the wind noise. The amplitude and phase responses of the I23FR WNRS were calculated, following the methodology of Gabrielson (2011) (brown lines within Figs 2b and c, Supporting Information S2). The resonance peak of the WNRS is expected to be around 6.6 Hz according to Alcoverro & Le Pichon (2005).

One of the main assumptions for data processing of the infrasonic wavefield is similar conditions at each array element (Shumway 1971; Brachet *et al.* 2010). This includes a coherent sound wave front impinging the array, while each element encounters similar Gaussian-white-noise conditions. The installation of identical measurement systems theoretically secures this assumption. In reality, however, the array elements are not always similar nor experience similar noise conditions. Defects in the WNRS or different locations of array elements cause a difference in local noise conditions, which leads to variances in the outcome of the data processing techniques.

3 METEOROLOGICAL CONDITIONS

The pressure spectrum of turbulence has been described statistically to decay with a slope of $f^{-5/3}$ (Gossard & Hooke 1975). This implies that the effect of wind noise increases towards lower frequencies (Raspet *et al.* 2019). Wind typically masks the background acoustic noise when turbulent processes in the lower atmosphere prevail at infrasonic frequencies. Various methods can be applied to reduce this wind-noise at infrasound arrays (Walker & Hedlin 2010; Raspet *et al.* 2019).

The meteorological conditions around an array give a first impression of the expected noise levels. The first element of the I23FR array includes a meteorological instrumentation to measure the horizontal wind, barometric pressure and temperature. The meteorological instruments are installed 2 m above the ground and sample at 1 Hz.

Meteo France operates and maintains a weather observation facility at a ∼ 1000-m distance from I2301. This facility measures

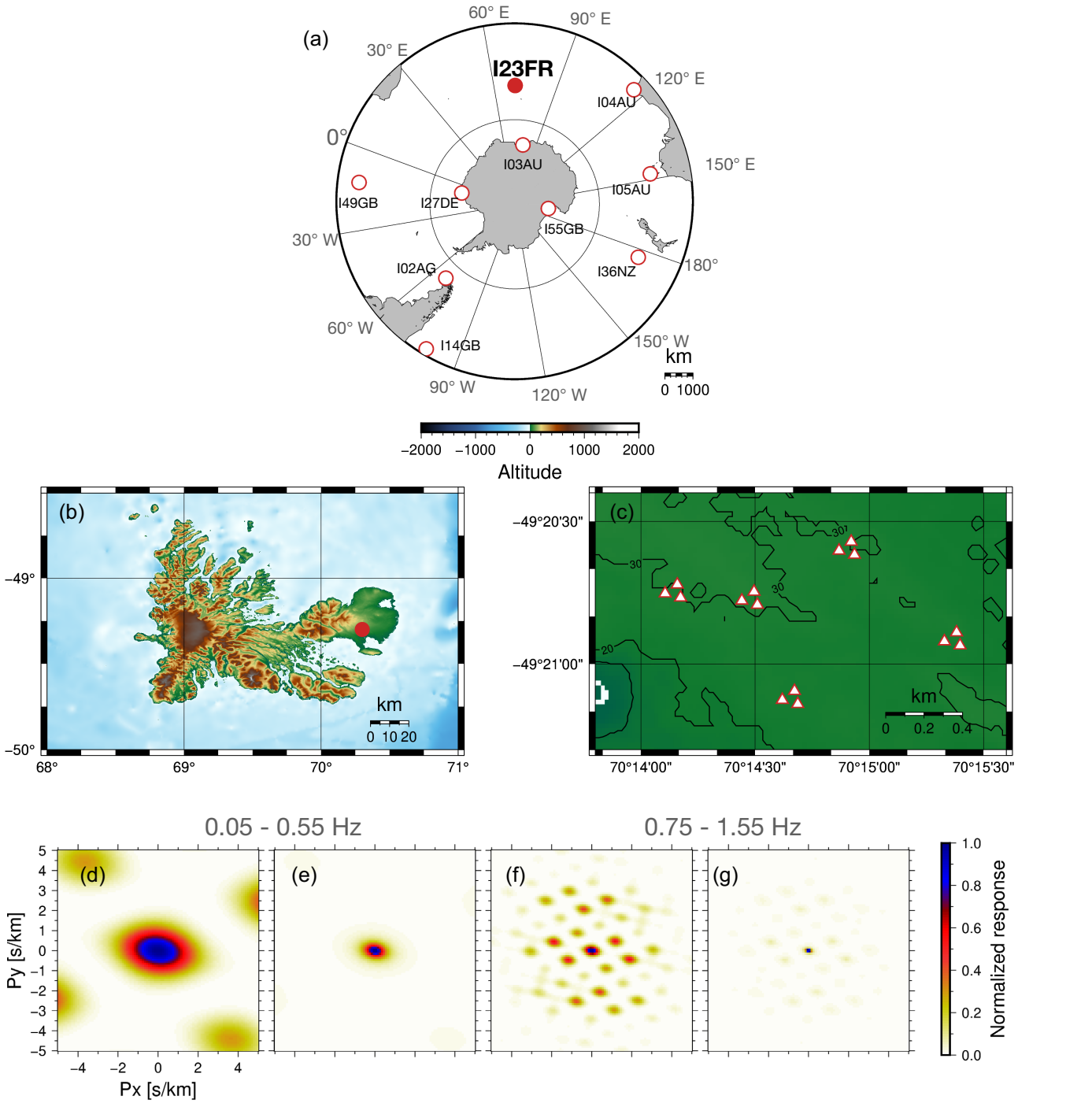

Figure 1. (a) An overview of Infrasound IMS arrays in the Southern Hemisphere. The solid red dot highlight the location of I23FR at the Kerguelen Islands. (b) The main island of the Kerguelen Islands and location of the infrasound array. (c) Positions of the 15 microbarometer elements (triangles) of the I23FR array, divided into five triplets. (d) and (e) show the array response of I23FR, based on Bartlett (1948) and Capon (1969), respectively, for the frequency ranges 0.05–0.55 Hz. (f) and (g) represent the responses for the frequency range 0.75–1.55 Hz.

the same meteorological parameters, as hourly synoptic observations (SYNOPS). The meteorological station of Meteo France is part of the Global Telecommunication System (GTS) of the World Meteorological Organization (WMO) (Panel 2005) and provides near real-time weather information. The meteorological observations are therefore WMO certified, meaning the measurements are performed at an elevation of 10 m above the ground.

Since the Meteo France and IMS facilities are not located at the exact same geological position, and measure at different heights, a a direct comparison is not correct. However, since the IMS and Meteo France measure similar weather parameters, a comparison to conclude on the use of the IMS observations is useful. Especially since the IMS's sample rate (1 Hz) is favorable compared to hourly SYNOPS observations by Meteo France.

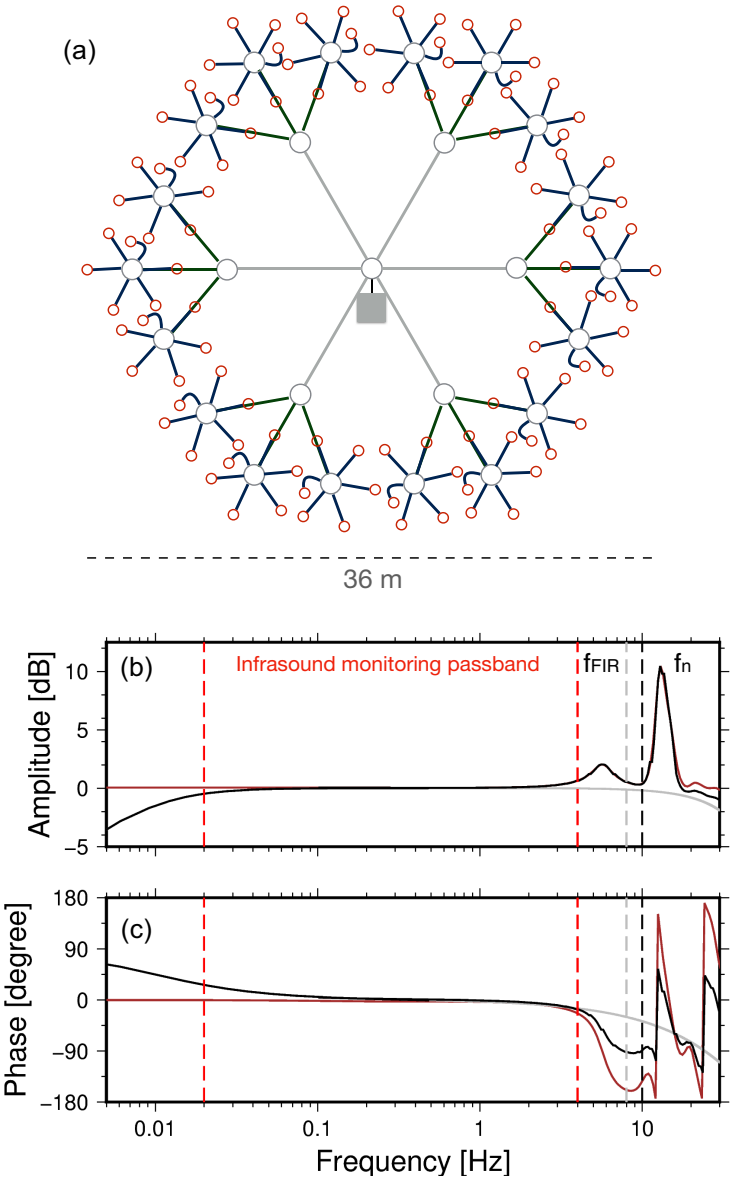

Figure 2. (a) A model of the WNRS featuring 18 pipe rosettes, which is applied to all microbarometers (centre) of the I23FR array. (b) and (c) the amplitude and phase response of one array element (solid black line), which is based on the response of the microbarometer equipment (solid grey line) and the response of the WNRS (solid brown line). The red dotted lines indicate the monitoring passband for the CTBT (Marty 2019). The black dotted lines indicate the Nyquist frequency (f_n) of I23FR, and the grey dotted lines indicate the limit above which the data should not be utilized due to the effects of the analogue-to-digital converter filters ((Sleeman *et al.* 2006), f_{FIR}).

Table 1. Specifications of the WNRS system applied to I23FR.

WNRS I23FR			
Length pipe$_1$	$l_1 = 10.27$ m	Diameter pipe$_1$	$a_1 = 15$ mm
Length pipe$_2$	$l_2 = 5.13$ m	Diameter pipe$_{2,3}$	$a_{2,3} = 8$ mm
Length pipe$_3$	$l_3 = 2.56$ m	Summation cavity volume	$a_2 = 1e^{-3}$ m
Length pipe to sensor	$l_s = 3$ m	Length pipe to sensor	$a_s = 8$ mm

Besides *in-situ* meteorological measurements, ECMWF ERA5 atmospheric reanalysis data are used in this study. ERA5 offers a high-resolution realization (HRES) and a reduced resolution ten-member ensemble (EDA). The ERA5-HRES is available per hour and has a spatial resolution of 0.36°. The ERA5-EDA has a spatial resolution of 0.5° and a temporal resolution of 3 hr. The Southern and Indian Oceans surround Kerguelen Island. Therefore, rapid changes in atmospheric variables are expected. The ERA5 EDA is applied within this study to exclude outliers from individual ECMWF members (Era5 reanalysis 2017).

3.1 Analysis of Meteorological ground observations

In this section, a comparison between the three different meteorological data sets for Kerguelen Island is made over five years of data (2015–2020).

The left-hand column of Fig. 3 shows the comparison between ERA5 and *in-situ* observations at I23FR. For this comparison, daily means of the meteorological data have been determined for both data sets. The middle column compares the *in-situ* observations measured at the Meteo France and I23FR meteorological stations. Here, hourly means have been used for comparison. The right-hand column indicates the monthly averages of the I23FR meteorological observations. The differences and standard deviations are shown in Fig. 3 and listed in absolute values within Table 2. It stands out that there is a good agreement between the *in-situ* data measured by Meteo France and I23FR.

3.2 Analysis of vertical ECMWF profiles above Kerguelen Island

Besides local noise conditions, vertical profiles give insight into the atmospheric propagation conditions of infrasonic signals. Infrasound can propagate over large distances facilitated by acoustic waveguides, that can form between the Earth surface and various altitudes throughout the atmosphere, depending on the temperature and horizontal wind conditions. These waveguides change with time and location. The effective speed of sound ratio is a practical measure to quantify favourable ducting conditions. As the interest in this study is with ground-based sources, ground-to-ground ducting conditions are considered. For this, the effective sound speed ratio is normalized to the sound speed at the ground surface. An effective sound speed ratio near or greater than one indicates that infrasound can propagate efficiently in a waveguide.

The effective sound speed approximates the combined effect of wind, temperature (T), and the specific gas constant ($R_{\text{air}} = 287\,\text{J}\,\text{kg}^{-1}\,\text{K}^{-1}$) on infrasound propagation. The effective sound speed (C_{eff}) is defined as the sum of the adiabatic sound speed ($C_t = \sqrt{\gamma R_{\text{air}} T}$) and the wind in the direction of propagation (Drob 2019; Assink *et al.* 2019) for a fixed horizontal position and time:

$$C_{\text{eff}}(z,\theta) = C_t(z) + \mathbf{W}_{xy}(z)\cdot\hat{n}_{xy}(\theta) \tag{1}$$

where $\mathbf{W}_{xy}(z)\cdot\hat{n}_{xy}(\theta)$ indicates the horizontal winds at altitude z in sound propagation direction θ. The vertical variation in $C_{\text{eff, ratio}}$ indicates the refractivity of the atmosphere and is defined as the ratio of the effective speed of sound at an altitude z and at the ground, equal time and location:

$$C_{\text{eff, ratio}}(z,\theta) = \frac{C_{\text{eff}}(z,\theta)}{C_{\text{eff}}(0,\theta)} \tag{2}$$

Fig. 4 shows the climatology of the meteorological parameters that are relevant for infrasound propagation, derived from the ERA5-EDA. From this figure, the various waveguides within the atmosphere become clear. ERA5 resolves atmospheric model data up to 80 km altitude. The tropopause (∼10 km), stratopause (∼50 km) are visible within this figure. The mesosphere and lower thermosphere is not resolved by the ECMWF model. However, these regions make up the upper layers of the thermospheric waveguide. This duct always exists due to the strong temperature gradient around the mesopause region (Drob *et al.* 2003; Waxler & Assink 2019), but is less efficient for long-range propagation because of the increase in acoustic attenuation at these altitudes (Sutherland & Bass 2004). Nonetheless, from the figure, it stands out that the stratospheric duct is dominant.

Fig. 5 shows the effective sound speed profiles at I23FR for four different periods and backazimuths. The summer, autumn, winter and spring profiles are represented by ECMWF ERA models for the first day of 2015 January, May, July and October, respectively. The blue lines indicate the effective sound speed profiles, whereas the grey areas indicate whenever a specific angle has a $C_{\text{eff, ratio}}$ greater than one. From this figure, it stands out that during the austral summer (January), an easterly stratospheric duct occurs within the atmosphere. Infrasonic signals will most likely be propagated from the east to the west. In contrast, during the austral winter (July), a westerly stratospheric duct occurs in the atmosphere, signals will most likely propagate from the west to the east.

The thermospheric propagation conditions are causing a continuously effective speed of sound ratio greater than one (Figs 4 and 5), and thus a favourable ground-to-ground ducting condition. However, compared to stratospheric propagation the thermospheric propagation is less effective due to the high thermo-viscous absorption (Sutherland & Bass 2004).

4 INFRASOUND OBSERVATIONS

4.1 Ambient local noise

The meteorological conditions near the array provide insight into the infrasonic noise conditions (Fig. 3). From those observations, it can be stated that I23FR experiences winds stronger than 5 m s^{-1} all year round. Such harsh conditions may reduce the array's ability to detect coherent infrasound and estimate the parameters of interest as the infrasonic signals are masked by incoherent pressure perturbations from wind noise (Walker & Hedlin 2010).

Within this study, hourly power spectral densities (PSDs) are computed for each array element. The PSDs are aggregated into probabilistic power spectral density (PPSD) distributions that give insight into noise distribution as a function of frequency. Fig. 6(a) shows the PPSD of I23FR for 2015 until 2020 (excluding elements 12 and 14, which were unavailable during that period). The PPSD distribution shows that the noise conditions around I23FR are relatively high over the entire infrasonic frequency band, compared to the global high and low noise curves (Brown *et al.* 2014). These observations are in line with earlier observations by Brown *et al.* (2014) and den Ouden *et al.* (2021).

Besides the high noise levels, the resonance peak around 6.6 Hz stands out due to the system response function (Fig. 2). This feature can be suppressed from the spectra by deconvolving the system response from the spectra (Bracewell 1986), as shown in Fig. 6(b).

4.2 Triplet noise

Algorithms used to process infrasonic array data typically rely on the assumption that the background noise can be modelled as Gaussian stationary white noise with equal noise levels at all array elements. Moreover, the signal of interest is typically considered to be perfectly correlated over the array's aperture. To assess the detection capability of an infrasonic array, it can therefore be helpful to analyse the PSDs at each array element (Brachet *et al.* 2010; Green 2015). PSDs of individual elements are compared to determine the difference in noise conditions per array element. For each hour, the residual PSD is determined and plotted against the average wind direction and speed over that particular hour from the CTBT data

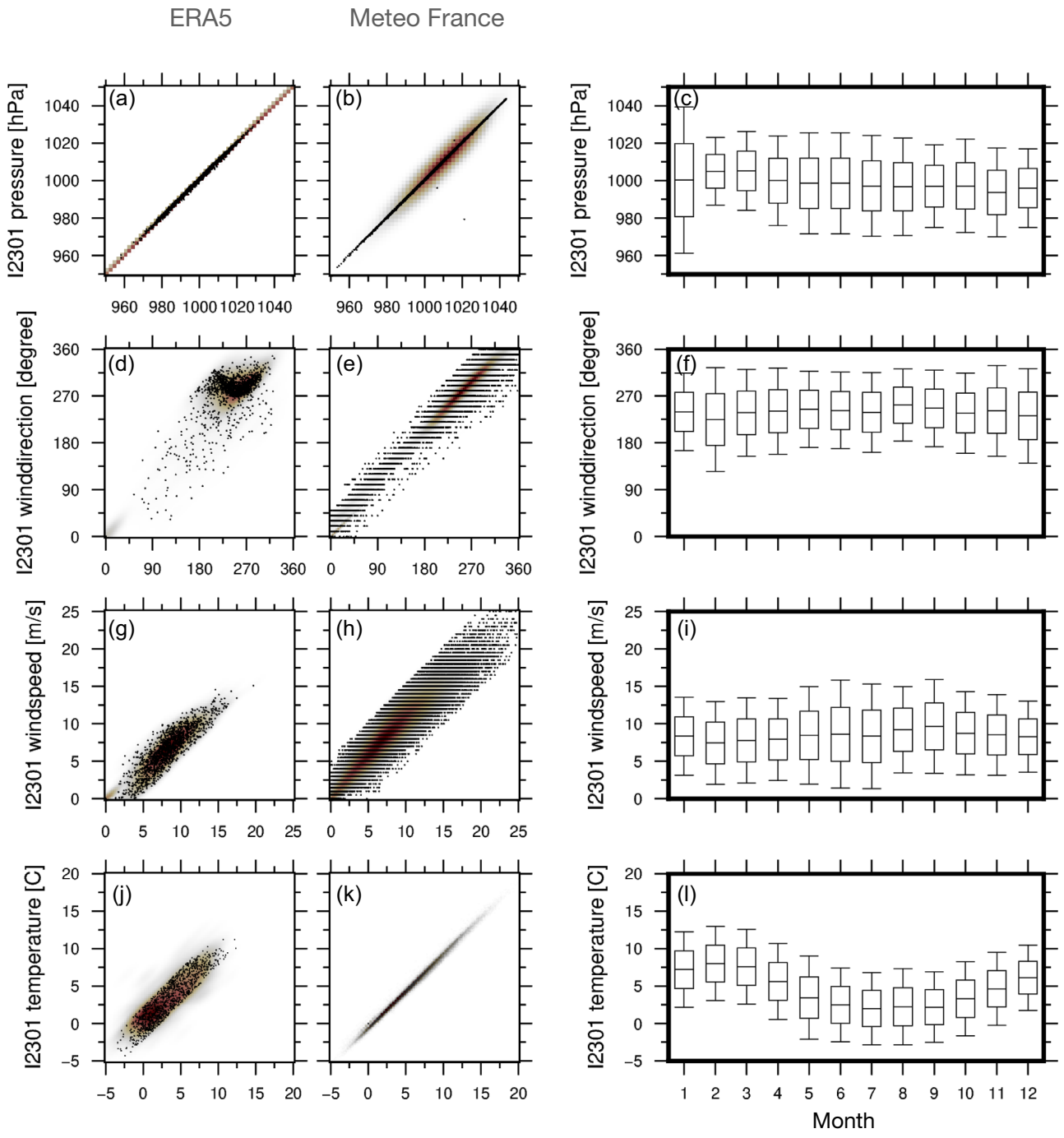

Figure 3. Meteorological observation and comparison at Kerguelen Island. The left-hand panels (a), (d), (g) and (j) compare 3-hr meteorological observations at I23FR with ERA5 EDA data. The middle panels (b), (e), (h) and (k) show hourly comparisons between between I23FR data and MeteoFrance. Overlayed on the data points the normalized distribution is shown. The right-hand panels show the monthly average with a 95 percentile error bar from 2015 until 2020.

(Section 3). The residual PSD is determined as:

$$\sigma_{\mathrm{PSD}}(f,t) = \sqrt{\frac{1}{N}\sum_{i}^{N}(\mathrm{PSD}_i(f,t) - \mu_{\mathrm{PSD}}(f,t))^2} \tag{3}$$

where PSD_i is the PSD of element i, N the number of elements and μ_{PSD} indicates the average PSD over the entire array.

The average residual has been calculated over the array recordings between 2015 and 2020 with a 99.9 percentile Gaussian distribution (Figs 6c and d). Note that the dominant wind direction is westerly (Fig. 3), which results in more data within that quadrant. It stands out that the omnidirectional residual between the elements PSDs is ∼1 dB. Although the array experiences harsh weather conditions and the PSD noise levels are relatively high (Fig. 6b), the difference in PSD between array elements is constant over various wind directions and speeds. The local noise conditions over the array elements are determined to be similar.

Table 2. Comparison of meteorological *in-situ* data of I23FR (2 m instrument height) and ECMWF ERA5 atmospheric re-analysis data (2 m height, left-hand column), and *in-situ* observations from MeteoFrance (10 m height, right-hand panel). Note that negative values indicate an underestimation by I23FR compared to ERA5/MeteoFrance, and positive values indicate an overestimation.

Meteorological comparison I23FR	
ERA5 2 m	MeteoFrance 10 m
Barometric pressure: -0.75 ± 0.68 hPa	Barometric pressure: 0.38 ± 0.69 hPa
Wind direction: $-7.21 \pm 4.01°$	Wind direction: $-3.87 \pm 1.57°$
Wind speed: 1.65 ± 1.38 m s^{-1}	Wind speed: -0.85 ± 0.07 m s^{-1}
Temperature: -0.01 ± 0.19 °C	Temperature: 0.72 ± 0.01 °C

This remark, however, does not express anything about the ability to resolve infrasonic signals. However, it does state the differences in local noise conditions over the array. It is a measure for local noise over an array, which is an important observation before applying data processing techniques.

4.3 Beamforming methods

Array processing techniques (e.g. beamforming) can separate the coherent parts of the infrasonic array recordings. The ability to detect and estimate the incident direction of the microbarom wavefield relies on the beamform resolution as quantified by the array response. The array response is determined by the beamform technique, frequency of interest and the array layout. Ideally, the array response function approximates a delta function that is unity for the slowness $\vec{p}_0$ of interest (typically chosen $\vec{p}_0 = 0$ s m^{-1}). However, because a limited number of array elements are used in practice, the array response function is described by a main lobe of a finite width and multiple side lobes (Evers 2008).

Often the Bartlett (1948) and Capon (1969) beamforming algorithms are applied. For the Bartlett, known as the 'classical analysis', the signal power is maximized by summing the phase-aligned spectral values. Capon's method is derived as a maximum-likelihood filter. Due to the filter design, the noise in the power spectrum is optimally suppressed while keeping a constant gain in the direction of interest. The array responses for I23FR while applying Bartlett and Capon are shown in the bottom panels of Fig. 1, for a vertically incident wave with $f_0 = 0.05$–0.55 and 0.75–1.55 Hz. Capon's responses (panels d and f) have a sharper main lobe compared to the Bartlett responses (panels e and g). Moreover, the amount and amplitude of the side lobes when applying Capon's method are significantly reduced (den Ouden *et al.* 2020).

Within this study, time- and frequency-domain array processing techniques (i.e. beamforming) are applied and compared. The microbarometer elements at I23FR continuously acquire infrasound measurements at a rate of 20 samples per second. To detect possible events of interest, beamforming can be performed in the time or the frequency domain, searching for correlated signals. The time-domain beamforming is performed by using the time-domain Fisher detector (Melton & Bailey 1957; Evers 2008), which enables to determine the dominant source contribution. The frequency-domain beamforming within this study is performed by Capon (1969) beamforming, which is used to calculate a *f*/*k* spectrum. A comparison between Capon and Bartlett array responses illustrates that the Capon method is a higher-resolution method than the Bartlett beamformer (Viberg & Krim 1997). As a post-processing method on the initial Capon spectrum, CLEAN beamforming has been applied (Capon-CLEAN, Högbom 1974). CLEAN allows for the identification of multiple infrasound signals within the same time and frequency window (den Ouden *et al.* 2020).

Both beamforming methods are applied in the passband of 0.05–0.55 Hz. The window size of both methods is 2000 seconds, with 90 percent overlap. The calculation of the *f*/*k* spectra occurs over a vector space spanned by steering vectors, which is formed by the slowness grid. The design of the slowness grid consists of a 360° ring grid plus a rectangular grid. The ring grid is a linear grid in backazimuth and apparent velocity, ranging from 0° to 360° and 285 to 500 ms^{-1} with steps of 2° and 1 ms^{-1}, respectively. This ring grid is nonlinear in the slowness domain. The rectangular grid consists of linearly spaced values between -0.005 and 0.005 sm^{-1}. This grid is added to ensure that energy from outside the ring grid does not clutter on its boundaries, which would result in biased outcomes. Within this study a Fisher detection threshold is used as a confidence interval for avoiding false alarms (Shumway 1971). The threshold depends on the array layout, frequency range and beamforming window size. The Fisher threshold is set to 1.19 in order to have a 95 per cent confidence on the resolved sources to be an actual signal instead of a false alarm.

4.4 Microbarom observations

Microbaroms are the most dominant infrasound sources detected worldwide and are the atmospheric counterpart of microseisms. The spectral peak of these signals is typically found around 0.2 Hz, but more generally, microbarom energy is detected in the 0.1–1.0 Hz band (Campus & Christie 2010; Landes *et al.* 2012; Hupe 2019). Both beamforming methods have been applied on the frequency band 0.05–0.55 Hz. The resolved infrasound signals within this frequency band are classified as propagating microbaroms, in contrast to evanescent microbaroms that are only present above the source (den Ouden *et al.* 2021).

Fig. 7 shows the outcome of the time-domain Fisher detector (a and b) and the frequency-domain Capon-CLEAN algorithm (c–e). The results show the expected seasonality in direction and apparent velocity. Note that both detectors have similar results. However, the CLEAN outcome contains more spatial information of the infrasonic sources since the CLEAN algorithm detects multiple spatially distributed sources within overlapping frequencies and time windows. Moreover, CLEAN gives insight into the frequency content of the resolved infrasound signals (panel e).

The beamforming outcomes show that the dominant infrasound signals in the austral summer are resolved from the east and in the austral winter from the west. Besides the seasonal change in the directivity of infrasound signals, the apparent velocity also changes with the seasons. The apparent velocities are higher in the austral winter than in the austral summer periods (Fig. 5). Furthermore, a frequency shift of the infrasonic wave front is revealed within the results. During the austral winter, microbaroms are observed over a wider frequency band, that also include lower frequencies (0.1–0.5 Hz) when compared to the summer (0.15–0.3 Hz). In addition, the amplitudes of the resolved microbarom signals change seasonally. During the austral winter the sound pressure level (SPL) of the microbarom is higher compared to the austral summer. This is due to the initial source power of the microbaroms, during winter the initial source power is higher, but also due to the propagation conditions during winter, which are favourable and therefore the microbarom signals will attenuate less during propagation towards the array.

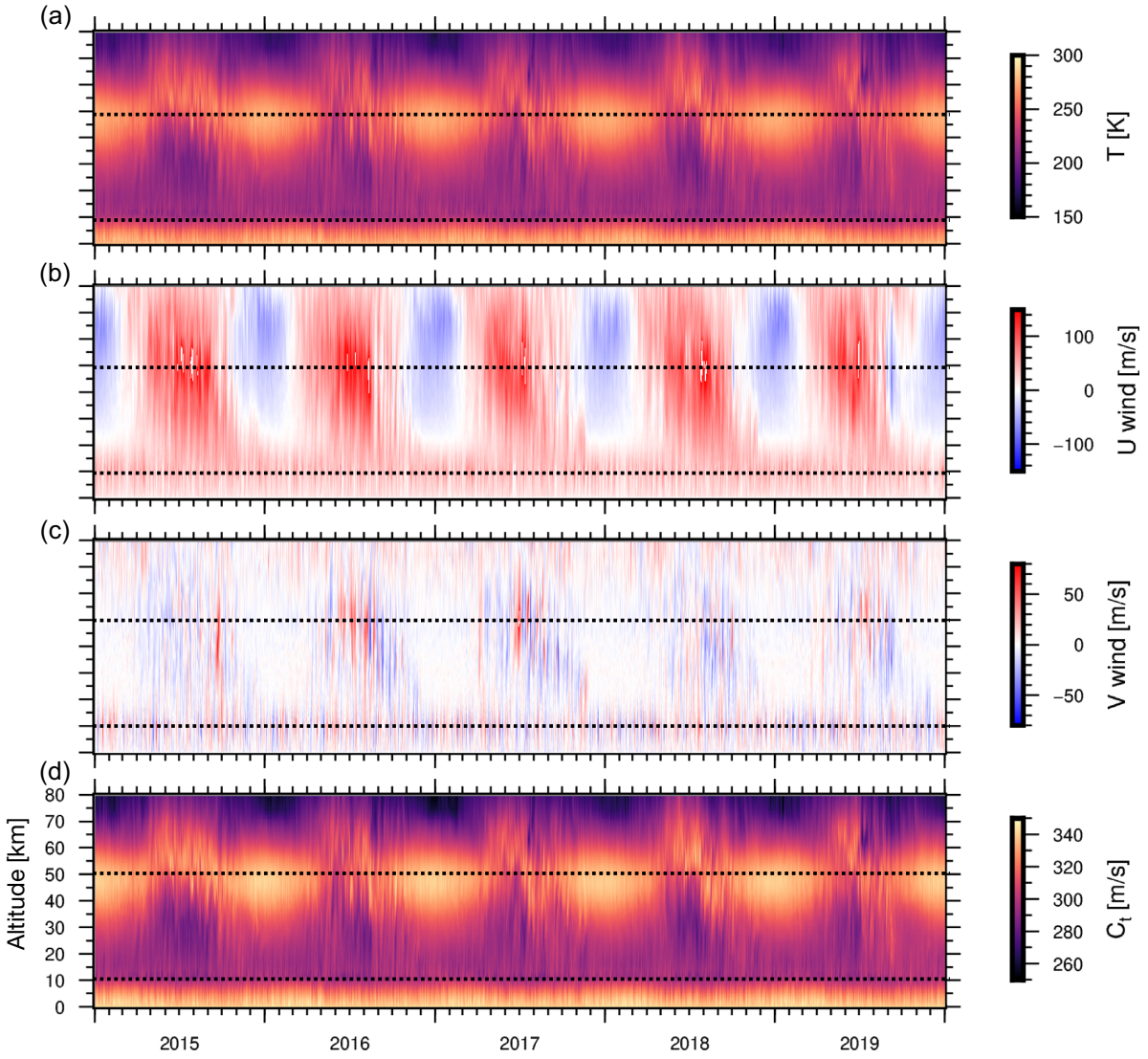

Figure 4. Vertical atmospheric profiles above I23FR derived from ERA5 data. As a function of time and geopotential height are shown: (a) temperature (K), (b) zonal wind ($m\,s^{-1}$), (c) meridional wind ($m\,s^{-1}$) and (d) adiabatic sound speed ($m\,s^{-1}$). The black dotted lines indicate the tropopause ∼10 km, and stratopause ∼50 km.

5 SIMULATING MICROBAROM SOUNDSCAPES

den Ouden *et al.* (2021) presented a method for the reconstruction of microbarom soundscapes. Such soundscapes account for all omnidirectional propagating microbarom source contributions and present microbarom spectra in absolute values. The computed acoustic intensities are integrated over the ocean surface, based on a microbarom source model (Waxler *et al.* 2007), and accounts for long-range propagation (Tailpied *et al.* 2016).

In the literature, there are various studies that compare infrasonic microbarom observations and microbarom source region models (Landes *et al.* 2012; De Carlo *et al.* 2020; Vorobeva *et al.* 2020; Šindelářová *et al.* 2021). Typically, array processing techniques are applied to detect the dominant microbarom signal and direction in a given time segment and frequency band. Therefore, only the resolved direction and amplitude of this dominant microbarom observation is compared with microbarom models. However, Assink *et al.* (2014) and Smets & Evers (2014) have shown that multiple spatially distributed sources within the same time segment and frequency often occur.

For the computation of soundscapes, the microbarom source model is calculated with the use of the 2-D wave spectra (2DFD) that are computed by the ECMWF ERA5 Wave Action Model (WAM). The 2DFD field is available at 30 oceanic wave frequencies spaced exponentially between 0.035 and 0.5476 Hz and 24 wave directions, linearly spaced over 360°. This 2DFD reanalysis is coupled to the atmosphere model, which allows interaction between the ocean waves and the surface winds (Haiden *et al.* 2018). The reanalysis has an hourly output, with a spatial resolution of 0.36°. The transmission loss from each position in the grid to the infrasound array location at Kerguelen island is computed using the empirical relation proposed by Tailpied *et al.* (2016). This relation extends the original methodology by Le Pichon *et al.* (2012) for range-dependent atmospheres. This class of empirical propagation loss

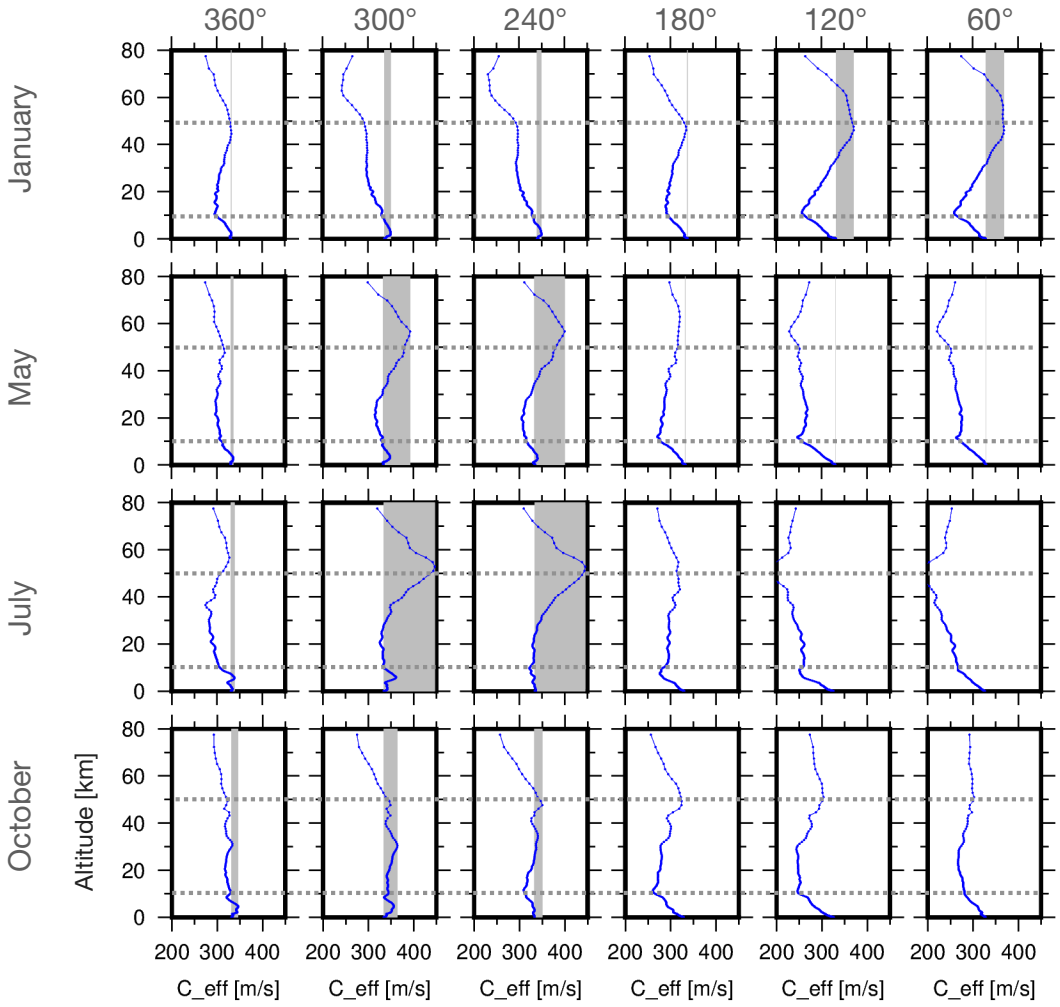

Figure 5. Effective sound speed profiles at Kerguelen Island for different periods and backazimuth directions. The grey areas indicate when the effective sound speed is above one. The grey dotted lines indicate the tropopause ∼10 km, and stratopause ∼50 km.

functions is derived as a functional fit to transmission loss curves computed using the Parabolic Equation (PE) method (Le Pichon *et al.* 2012).

An example of a soundscape analysis for the four different seasons considered in this study is shown in Fig. 8. The panels on the top row show the initial microbarom source region model as derived by Waxler *et al.* (2007) and implemented by Smets (2018) for summer (left-hand column), autumn (middle-left column), winter (middle-right column) and spring (right-hand column). The middle row panels indicate the long-range propagation conditions within the atmosphere, where the vectors describe the strength and direction of the stratospheric winds (Fig. 4). The panels on the bottom row show the interpolated microbarom soundscapes from the perspective of I23FR, integrated between 0.05–0.55 Hz. The microbarom soundscapes illustrate the source regions that potentially have been detected at the array. Note that the microbarom soundscapes change significantly with the seasons. While the sources are centred around the island for the May and October cases, there is a strong directional difference of microbarom source regions between January and July due to the propagation conditions (Fig. 5). During the austral summer and winter a strong easterly and westerly stratospheric propagation duct is expected. These propagation ducts weaken during the autumn and spring, when the middle atmospheric winds reduce as the circumpolar vortex reverses direction. This results in a omnidirectional spread of microbarom source regions that can be sensed by I23FR.

5.1 Spectral analysis

The soundscapes can be used to create omnidirectional PSDs of the spatial distribution of microbarom source regions around I23FR:

$$\mathrm{PSD}_{\mathrm{synth}}(f,t) = \sum_{\theta_i}^{\theta} \sum_{S_i}^{S} \mathrm{SPL}_{\mathrm{Synth}}(f,t,\theta_i,S_i) \tag{4}$$

where f represents the frequency, t the time period, θ_i the directional angle and S_i the distance within the stereo-graphic polar grid.

Synthetic PPSDs indicate the expected SPL contributions of microbaroms from a model perspective. The PSDs are calculated with a time resolution of one hour, over the entire frequency range (0.069–1.095 Hz) of the soundscapes, aggregated and displayed as PPSDs.

Fig. 9 shows the synthetic PPSD for I23FR, using five years of data between 2015–2020. The grey solid lines indicate the global high and low noise curves (Brown *et al.* 2014). By comparing this synthetic PPSD with the PPSD obtained from the *in-situ* measurements (Fig. 6b), it becomes clear that there is a difference in spectral power. Note that I23FR experiences extreme meteorological conditions (Section 3). Therefore, in the comparison of these spectra the

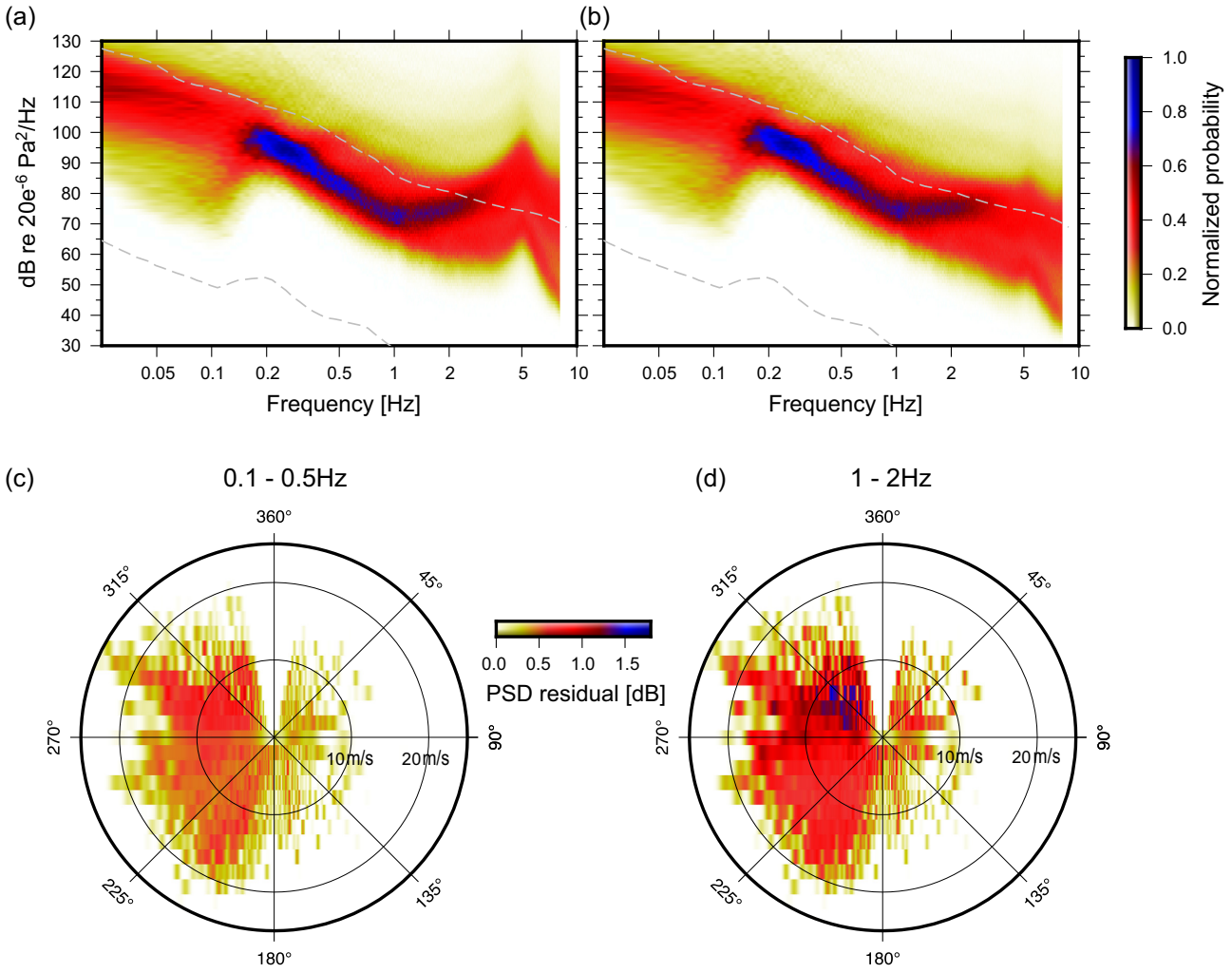

Figure 6. PPSDs computed for five years of I23FR data. PPSDs are computed for I23FR sensor data (except elements 12 and 14, which were unavailable during that period) (a) without and (b) with correcting for the WNRS response (Fig. 2). Panels (c) and (d) show the power difference between individual array elements of I23FR under varying meteorological conditions (wind speed and direction) for 0.1–0.5 and 1–2 Hz, respectively.

synthetic soundscapes only account for remote microbarom contributions. Local coherent and incoherent noise around the array are neglected. In particular the 95 per cent percentile PPSD is likely determined to a great extent by local turbulence in the vicinity of the array and not by microbarom noise levels. Therefore, the 95 percentile PPSD of the recordings can not be directly compared with the synthetic PPSD. The median level PPSD of the I23FR observations (Fig. 6b) shows a better agreement, especially for the higher frequencies (∼0.3–0.8 Hz). Nevertheless, the typical 0.2 Hz microbarom peak is moderately visible due to the lower SNR values compared to microbarom spectra that are typically observed at (IMS) infrasound stations (Marty 2019). This is most likely due to the high noise conditions experienced within the recordings of I23FR compared to the other IMS arrays (Section 3). In the synthetic PPSD, this wind noise contribution is not taken into account. The 5th percentile PPSD level corresponds to periods of low noise conditions. Therefore, this curve can be used to compare against the synthetic PPSD. Both show similar SPL's while resolving the characteristic microbarom amplitude signature around 0.2 Hz (Campus & Christie 2010). The wind-noise effects on microbarom recordings decrease at increasing frequencies (Gossard & Hooke 1975).

5.2 Seasonal effects

The seasonal effects on microbarom signal propagation depend on the atmospheric conditions (Figs 4 and 5). The detectability of the most dominant microbarom source is highly influenced by these conditions (Fig. 8). A similar analysis as time-domain Fisher beamforming can be performed using microbarom soundscapes. Fig. 10(a) shows the characteristics of the most dominant sources within the microbarom soundscapes. Those soundscapes are calculated for each hour of model output and created between 2015–2020 from the perspective of I23FR. From this outcome, it becomes clear that the most dominant source contribution from the soundscapes changes with the seasons. During the austral summer (January), the east is the dominant source direction, while during the austral winter (July), the sources propagate from the west.

Besides resolving the most dominant source contribution, an analysis similar to CLEAN beamforming can be performed. For each soundscape, the total SPL has been determined. Based on the total SPL, a directivity and frequency study has been performed. From the perspective of I23FR, the total soundscape field is divided up by direction. The cones that describe the directions are described by a Gaussian distribution, centered around a mean direction and a

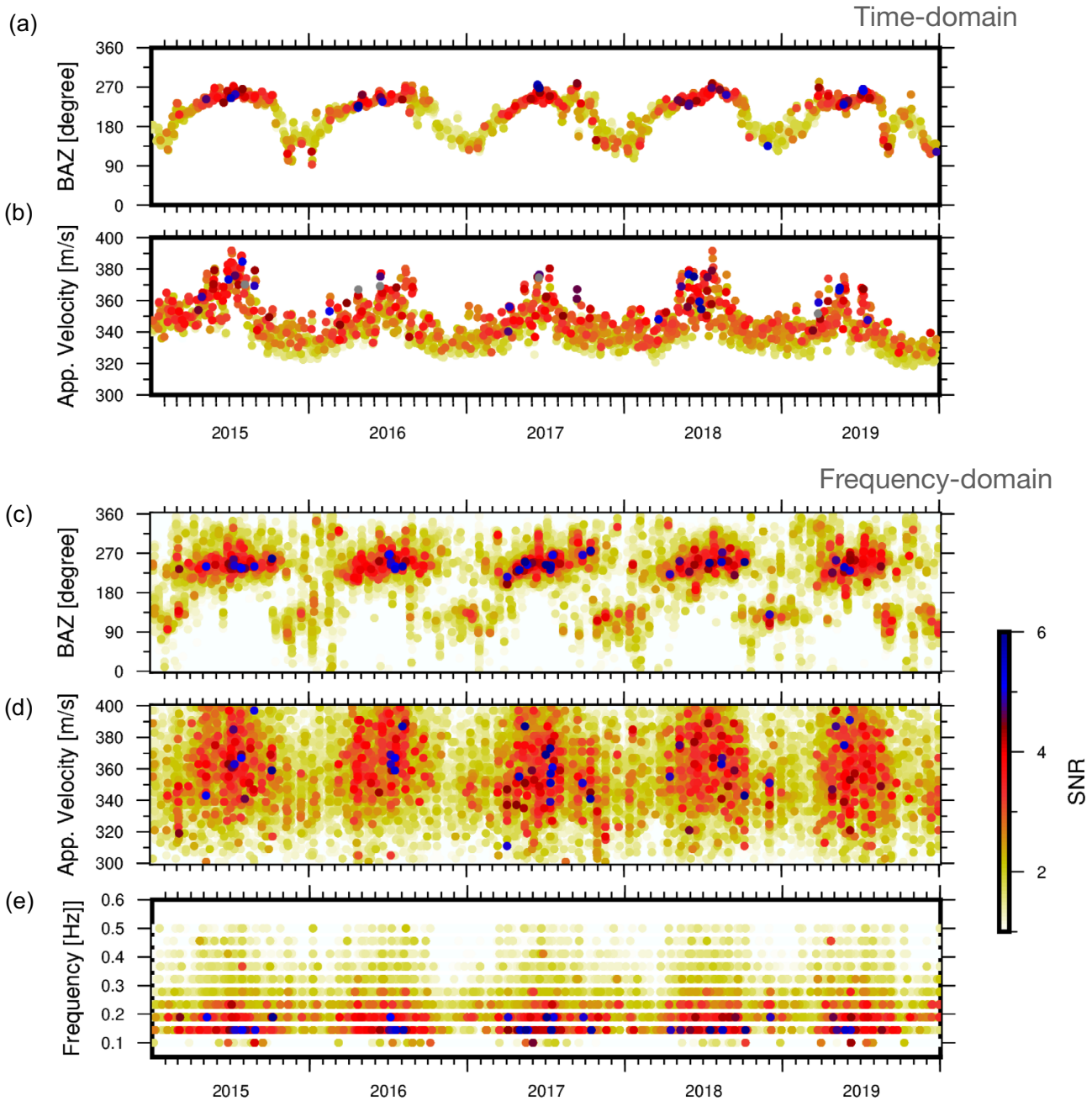

Figure 7. The outcome of the time-domain Fisher (panels a and b) and the frequency-domain CLEAN beamforming analysis (panels c–e).

standard deviation of 10°. Each cone has an overlap of 5°. For each cone, the SPL is determined. A threshold of 5 per cent of total SPL has been used. Figs 10(b) and (c) show the outcome of this analysis. The outcome presented in panel (b) shows a similar season pattern as in panel (a). However, accumulating multiple source contributions results in a more insight into the spatial microbarom contributions. Microbarom source regions are often dynamic and largely spread out (∼10000 km^2). The most dominant microbarom contribution, therefore does not always correctly represent the actual infrasonic wavefield. Besides the directional analysis of microbarom source regions from the soundscapes, frequency analysis can be performed. Panel (c) shows a spectrogram of the accumulative microbarom source region contribution from panel (b). This analysis shows that the microbarom source contributions during the austral winter (July) have a lower frequency content than the austral summer (January). Moreover, the distribution of frequencies is wider during the austral winter.

5.3 I23FR microbarom exposure

Besides directional and frequency information of microbarom source regions, the soundscapes also enable the construction of cumulative probability distributions to quantify the exposure of the array to microbarom source energy. The smallest area that encloses 95 percent of SPL generation has been determined for each soundscape, and is parametrized by the largest distance to the boundary of this area (Fig. 11a, black dots). The most dominant source contribution is always located considerably closer to the array (at ∼250 km

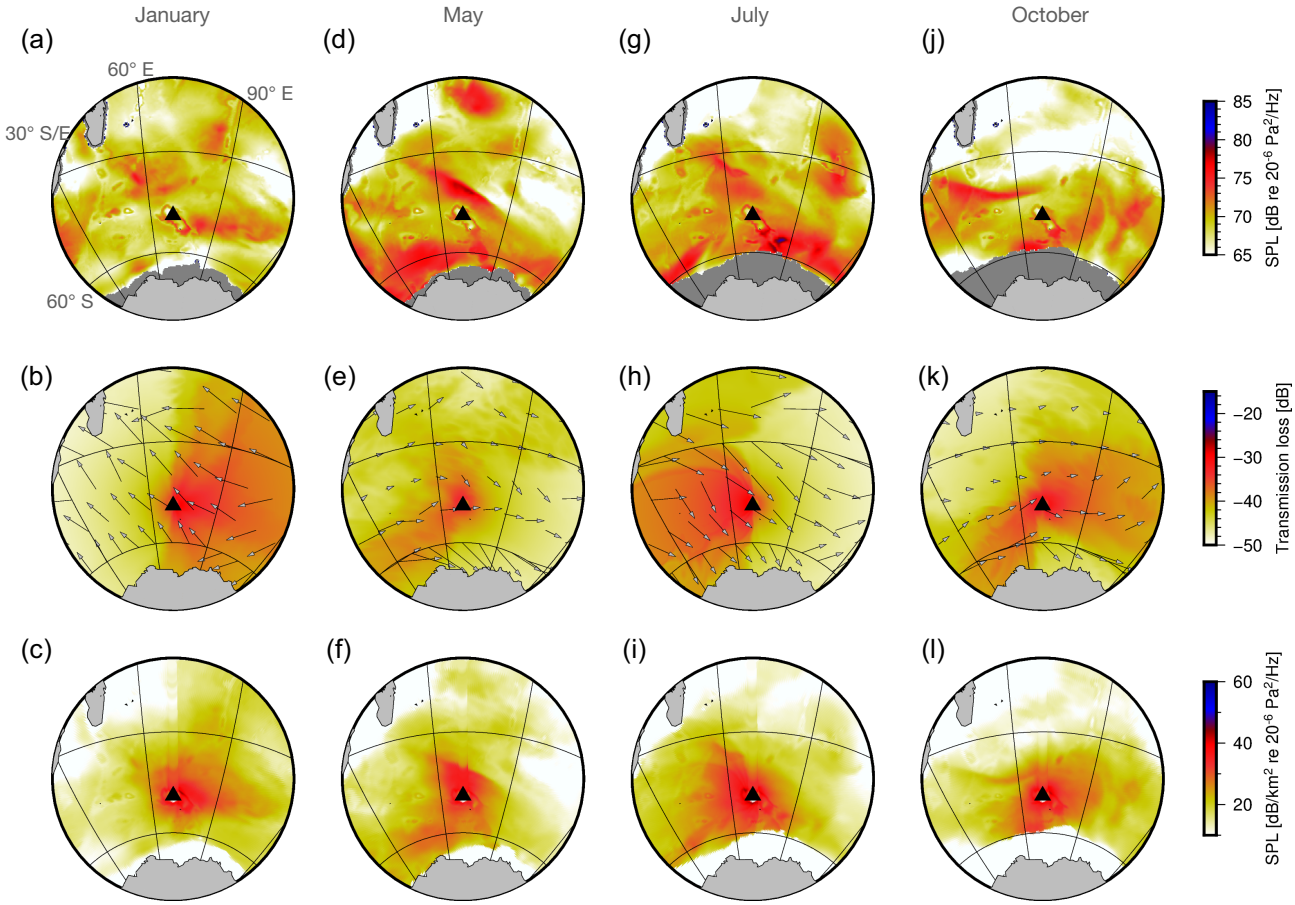

Figure 8. Synthetic soundscape reconstruction of the infrasonic wavefield around I23FR, integrated between 0.05–0.55 Hz. The top panels (a), (d), (g) and (j) show the initial microbarom source region model for summer (left-hand column), autumn (middle-left column), winter (middle-right column) and spring (right-hand column) conditions. The middle panels (b), (e), (h) and (k) indicate the long-range propagation conditions within the atmosphere, where the vectors describe the magnitude and direction of the stratospheric winds (∼30 km altitude). The bottom panels show the interpolated microbarom soundscapes.

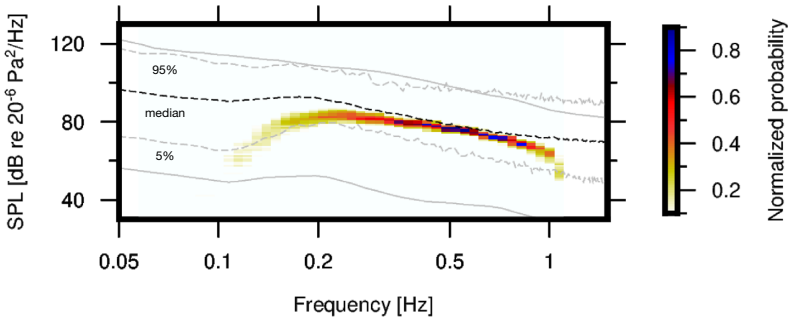

Figure 9. Synthetic PPSD of the soundscapes for I23FR. The grey solid lines indicate the global high and low noise curves (Brown *et al.* 2014). The grey and black dotted lines present the 5 and 95 percentile and the median curve of the observed PPSD levels at I23FR (Fig. 6).

distance, Fig. 11a, red line). From this analysis, it is concluded that the SPL contributions by microbaroms at I23FR are from source regions within an area that has an approximate radius of 2000 km.

Nevertheless, the SPL percentile analysis is relative. During the austral winter the propagation conditions and the microbarom source areas are favourable for higher SPL levels (Figs 7 and 10). Fig. 11(b) shows the omnidirectional SPL contribution of the microbaroms over distance in absolute numbers. From this panel it becomes clear that the exposure of microbaroms around the array is changing with the seasons. While the 95 percentile distance is of the same order of magnitude, I23FR is exposed to higher microbarom levels during the austral winter.

5.4 Comparing *flk* analysis to soundscapes

In this study, a climatology of the infrasonic wavefield around Kerguelen has been studied by using (1) *in-situ* infrasound data from array I23FR and (2) synthetic infra-soundscapes. Two beamforming

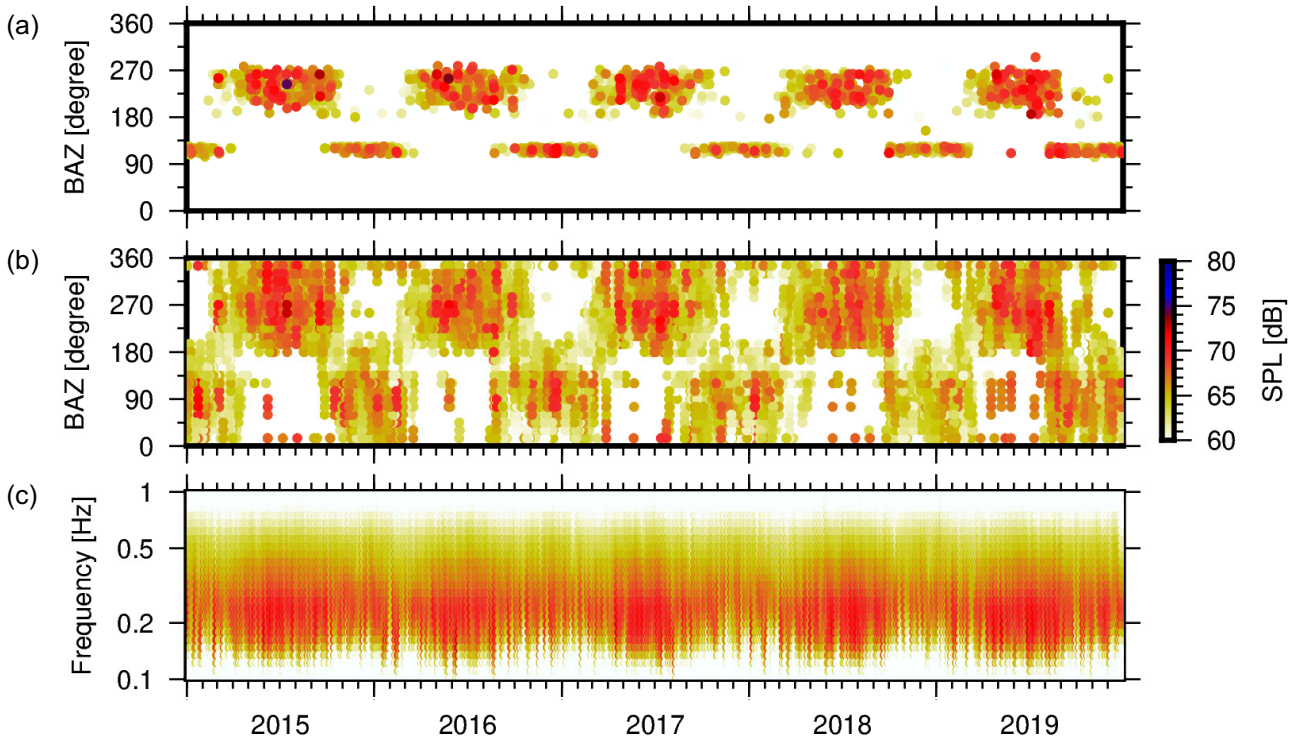

Figure 10. Seasonal SPL analysis of the synthetic soundscapes. Panels (a) shows the characteristics of the most dominant sources within the microbarom soundscapes. Panel (a) indicates the resolved backazimuth. Panels (b) and (c) show the outcome of the omnidirectional analysis of the soundscapes. The soundscapes have been divided into 10° cones, for which the SPL has been determined. Whenever the SPL is above 5 per cent of total SPL, it has been included within the figure. Panel (b) indicates the directionality, and panel (c) the frequency content.

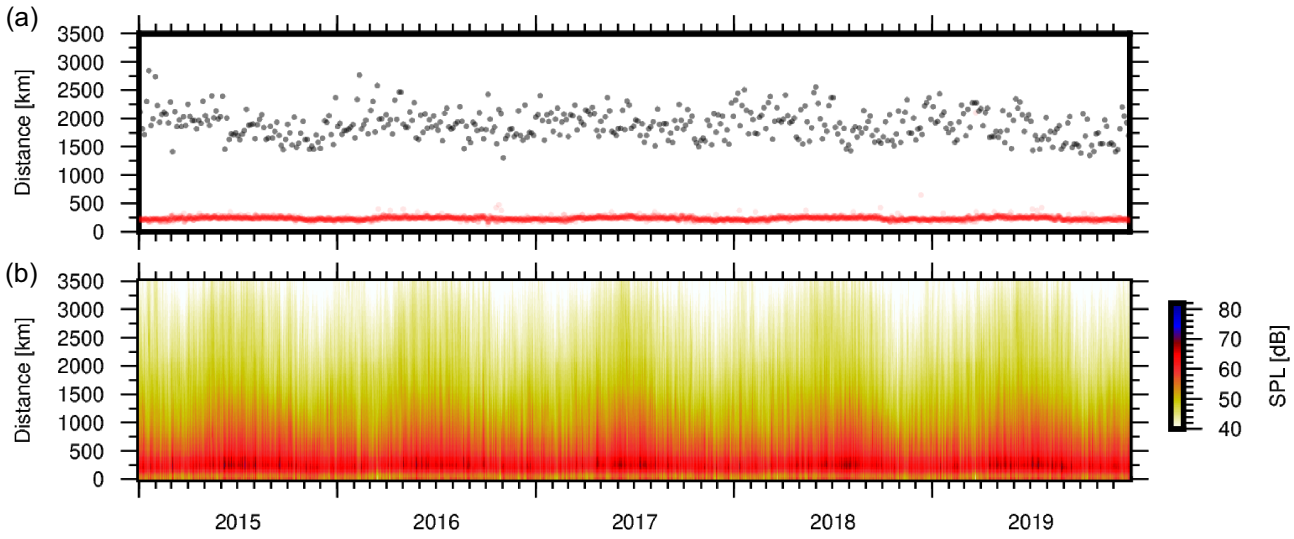

Figure 11. (a) The cumulative probability distribution of I23FR, which quantifies the exposure of microbaroms around the array. The black dots indicate the radius of the area which encloses the 95 percentile of the resolved SPL. The red dots correspond with the radius of the area of the most dominant source contribution within the soundscapes. (b) The microbarom SPL distribution at I23FR over radius.

methods, that is, time-domain Fisher and frequency-domain Capon-CLEAN, have been used to estimate the directivity, frequency content and amplitude spectra of coherent infrasound between 0.05–0.5 Hz.

Fig. 12 shows a comparison between beamforming results and the synthetic soundscape for 2015 October 01 at 00 UTC. Panels (a) and (b) show the *f*/*k* spectra of the initial Capon beamforming result and after applying CLEAN, respectively. Panels (c) and (d) show a similar analysis based on Bartlett beamforming. Below the *f*/*k* spectra, the corresponding soundscape for the same period is plotted. Within the soundscapes, the direction of the dominant source contribution from the beamforming observations is plotted (black arrow) and the CLEAN results (grey cones). The resolved dominant source direction by Capon-CLEAN points towards the dominant source contribution of the soundscape. Moreover, note that the initial *f*/*k* spectrum of Capon beamforming is of a

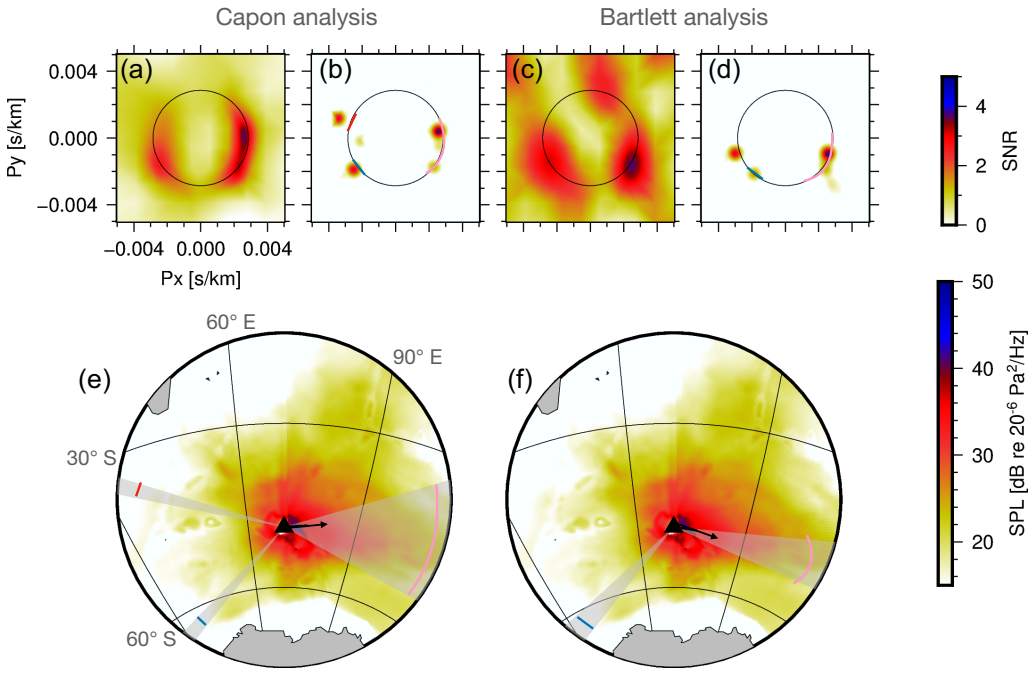

Figure 12. A comparison between beamforming results and synthetic soundscape for 2015 October 01 at 0 UTC. (a) and (b) show the *f*/*k* spectra of the initial Capon beamforming result and the result after applying CLEAN. (c) and (d) show a similar analysis based on Bartlett beamforming. (e) and (f) present the corresponding soundscape. The direction of the dominant source contribution from beamforming (black arrow), and the CLEAN results (grey cones) are highlighted within the soundscapes.

higher resolution than the Bartlett spectrum, which results in a more accurate outcome of the CLEAN algorithm (den Ouden *et al.* 2020). The Capon-CLEAN beamforming results are in general agreement with the derived soundscapes outcome.

6 CLIMATOLOGY COMPARISON

In Section 5, it was shown that the beamforming results are in general agreement with the soundscape simulations. The comparison over time between observations and model has been divided into two analyses. The first comparison is between soundscapes and the time-domain Fisher results, based on the most dominant source signal. The second comparison is between the soundscapes and frequency-domain CLEAN beamforming results and accounts for surrounding microbarom sources.

The outcome of the first comparison (Fig. 13) shows that during the austral winter months (June until September), the agreement between model and observation of the dominant source contribution over the entire five years of comparison is within $\sim 10^{\circ}$, for 81 per cent of the time. During the entire period, however, the agreement is less. There is a remarkable mismatch between the soundscapes and observations during the solstice period and the austral summer months. During these periods, the atmospheric state is variable and since the soundscape reconstruction is limited to a PE propagation model these propagation effects may not be encountered.

Nevertheless, this first comparison is not complete. Various studies have made the comparison between the dominant infrasonic observations and model outputs (Landes *et al.* 2012; Vorobeva *et al.* 2020). However, microbaroms source regions are dynamic, fast-changing, and often extended areas from the perspective of a distant array. Therefore all sound contributions should be taken into account, instead of only the most dominant contribution. The second comparison, therefore, is based on the CLEAN beamforming results and the omnidirectional soundscapes. Both methods account for the omnidirectionality of infrasonic sources, which can be divided into directional Gaussian cones. The cones span a range of 10° while having a 50 per cent overlap. The resolved power within each cone can be assigned to the coherent part of the infrasonic wavefield.

Figs 14 and 15 show the 'cone' comparison between the soundscapes and CLEAN observations. The direction of the sources in the modelled soundscapes and array processing (CLEAN) results are in good agreement, and both approaches resolve seasonal variations (Figs 14a and b). However, the SPL differs $\sim$5 dB. Panel (c) indicates the difference in SPL between soundscapes and CLEAN related to backazimuth. Note that incoherent noise has not been taken into account while reconstructing the soundscapes. The CLEAN beamforming results do contain effects of incoherent noise and are therefore slightly biased. However, these incoherent noise effects are minimal for higher amplitude signals. The synthetic soundscapes are derived from model data, which are a smooth and unvarying representation of the reality. Rapid changes and local differences are not resolved within these models. Comparisons between model and observations will enable improvements to be made to the models.

Fig. 15 shows a similar analysis based on the frequency content resolved from both methods. Again a good agreement between soundscapes (a) and CLEAN output (b) is noted. The frequency content of the resolved infrasound sources between both is complementary. Both show a broad frequency distribution during the austral winter (July), including the finding of lower frequencies. The frequency distribution during the austral summer (January) is more narrow.

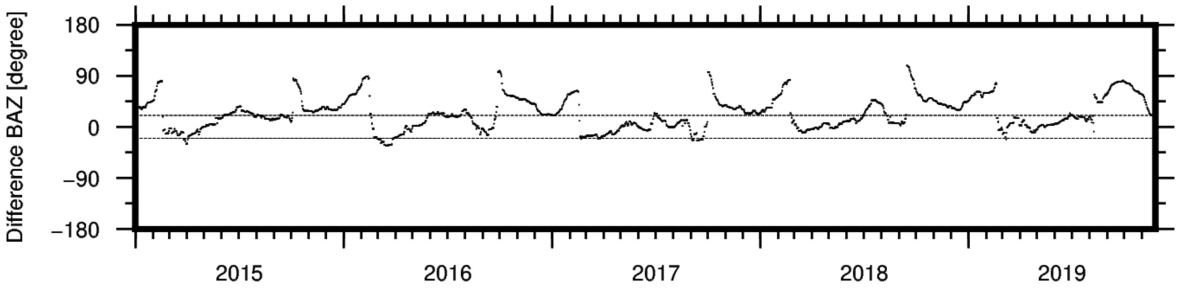

Figure 13. Comparison plot between the most dominant backazimuth direction resolved by the time-domain Fisher analysis (Fig. 7) and the soundscape reconstructions (Fig. 10). During the austral winter, there is a good agreement between model and observation. During the equinox and austral summer, the agreement decreases.

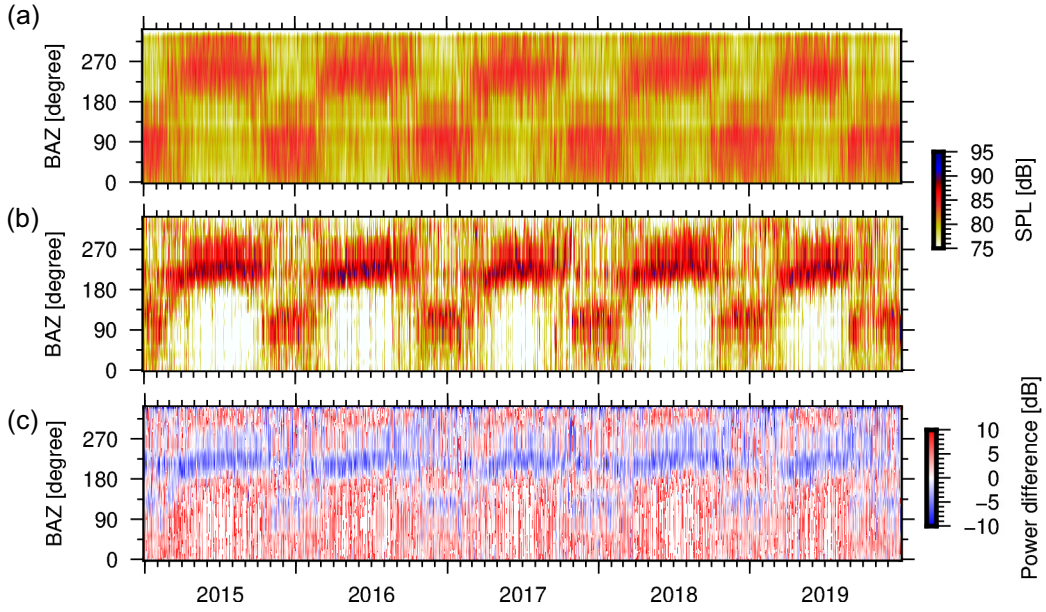

Figure 14. Comparison between directional synthetic soundscapes (a) and CLEAN observations (b). The panels show the SPL and backazimuth direction resolved from the soundscapes and CLEAN beamforming, where panel (c) shows a direct comparison between both in SPL.

7 DISCUSSION AND CONCLUSION

In this study, a climatology analysis of I23FR has been performed. This array is one of the microbarometer arrays of the IMS and provides real-time monitoring of the atmosphere (Marty 2019). The array is located at the Kerguelen Islands, positioned around the Indian and Southern ocean boundaries. Since the array experiences high ambient noise levels (Brown *et al.* 2014), it is often excluded from scientific studies. The climatology analysis presented in this study improves the general knowledge regarding the infrasonic wavefield received by the array. Various methods have been introduced and applied to unravel and characterize the wavefield into its individual components. The performed analysis is essential for the understanding of the infrasonic wavefield. The dominant source contribution is characterized as microbaroms, thanks to the frequency and amplitude signature (Campus & Christie 2010). Microbarom source regions are large areas from the perspective of distant arrays. The microbarom source component within the infrasonic wavefield has been analysed using observations and synthetic soundscapes. Microbaroms are often classified as ambient noise and may mask infrasonic signals of interest. A further understanding of the ambient noise field therefore comes to the benefit of infrasonic monitoring of nuclear tests and natural hazards.

Microbarom observations are analysed over five years using I23FR infrasound data by I23FR (2015–2020). Insight into the statistical distribution of microbarometer pressure spectra in terms of PPSDs is discussed in Section 4. These PPSDs contain both coherent infrasound as well as wind noise spectra. The microbarom peak can clearly be distinguished. The local noise conditions are high, relative to the global high and low noise curves (Brown *et al.* 2014). However, the difference in local noise conditions between the array elements is similar regardless of the wind direction and strength (Fig. 4). This analysis does not express anything about the ability to resolve infrasonic signals but can measure local noise consistency over the array. Similar noise conditions between array elements are essential when applying array processing routines, which typically rely on similar ambient noise conditions on the various array elements and a highly correlated infrasound signal.

Moreover, the infrasonic wavefield has been separated into coherent and incoherent parts by applying beamforming. Two beamforming methods (i.e. time-domain Fisher detection and frequency-domain CLEAN beamforming), have been applied to estimate the directivity and speed of the incoming coherent infrasonic wave front. Although the microbarom source regions seem close to the array (Figs 8 and 12), the sources can still be considered to be in the

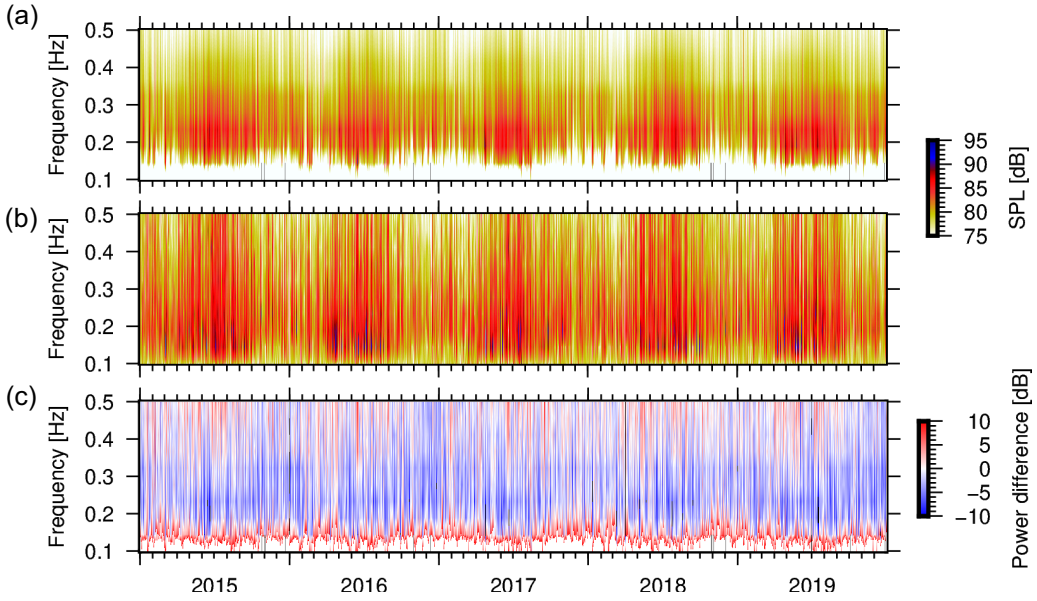

Figure 15. Comparison between the frequency content resolved from (a) the synthetic soundscapes and the (b) CLEAN beamforming. Panel (c) shows a direct comparison between frequency content of both expressed in SPL.

acoustic far field and therefore can be described by a superposition of plane waves. As a consequence, the CLEAN methodology as described by den Ouden *et al.* (2020) is still appropriate. CLEAN beamforming is a post-processing method on conventional data processing techniques (i.e. Capon beamforming). CLEAN iteratively deconvolves the array response of the most dominant source contribution from the data. The ability to resolve multiple microbarom sources therefore depends on the array response (Fig. 1). CLEAN divides the 'diffuse' Capon spectrum (Fig. 12a) into multiple point sources in the slowness domain (Fig. 12b, i.e. parametrized by azimuth and apparent velocity). In the case of microbarom processing, these point sources represent 'pseudo-microbarom point sources'. The point sources follow a Gaussian point spread function (PSF) described in Gal *et al.* (2016) and den Ouden *et al.* (2020). The diffuse Capon spectrum is therefore divided into microbarom source contributions. The width of the PSFs is user-defined and the functions serve merely as a tool to represent the separated source contributions in the slowness space. Whenever the initial f/k spectrum has a lower resolution, CLEAN will not separate the various microbarom contributions into these PSFs. Nevertheless, the representation of microbarom source regions as pseudo-microbarom point sources is merely an approximation, since microbarom sources are in reality spread out source regions. Microbarom classification as point sources suggests there is no correlation between two neighbouring sources (especially since the source region is relatively close to the array). Within Section 6, the first initiation of a non-point source microbarom analysis has been presented by dividing the CLEAN outcome into directional cones.

Besides the analysis of microbarom observations, the climatology involves the reconstruction of omnidirectional soundscapes from the perspective of I23FR (den Ouden *et al.* 2021). Section 5 describes the soundscapes and how to interpret results obtained from them. From the soundscapes, it stands out that the most dominant microbarom source regions are relatively close to the island (Figs 8 and 11), which may be the reason that the microbaroms are resolved clearly despite the very high wind noise levels. The microbarom signals are therefore significantly less affected by atmospheric propagation effects. A direct comparison between the dominant source contributions from soundscape simulations and observations is presented in Section 6. Within this section, a comparison method between soundscapes and CLEAN observations have been introduced and presented (Figs 14 and 15). The 'cone' partition transforms the resolved microbarom point source contributions of the beamforming detectors into microbarom source regions.

Although the comparison shows similarities in direction and frequency content, there is a notable SPL difference between observations and soundscapes. Within this study, the soundscapes only account for the theoretical contribution of microbaroms between 0.069–1.095 Hz. Additional source contributions within this frequency range are not taken into account. Furthermore, the beamforming outcome is affected due to the effects of incoherent noise within the recordings.

Moreover, within the reconstruction of the soundscapes, the transmission loss from each position in the grid to the infrasound array location at Kerguelen island is computed using an empirical relation (Le Pichon *et al.* 2012; Tailpied *et al.* 2016). This class of empirical propagation loss functions is derived as a functional fit to transmission loss curves computed using the PE method. This model can be used to approximate the losses due to propagation in a stratospheric duct, but is inappropriate to quantify losses due to tropospheric and thermospheric ducting. Furthermore, cross-winds are not taken into account by applying this propagation model. These winds influence the propagation conditions (Smets & Evers 2014; Assink *et al.* 2018; Blixt *et al.* 2019), which may explain the differences in dominant source angle between observations and soundscapes (Fig. 13). The use of formal propagation models requires atmospheric specifications from the ground to the upper atmosphere. As upper atmospheric specifications are typically limited to climatologies, this has implications for the accuracy of thermospheric returns (Assink *et al.* 2012; Drob 2019).

Nonetheless, the comparison between soundscapes and observations is promising. The soundscapes are generated from an initial

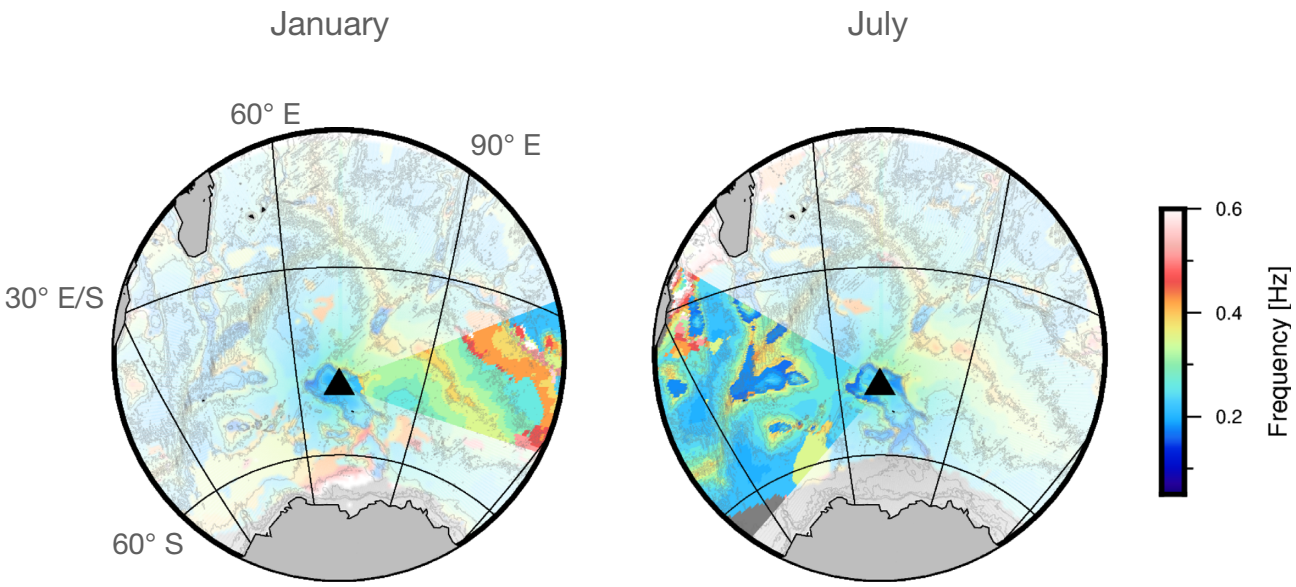

Figure 16. Spatial frequency analysis of two synthetic soundscapes during austral summer (a, 2015 January 01) and winter (b, 2015 July 01). The grey overlayed contour lines within the panels indicate the bathymetry from GEBCO 2020 (GEBCO 2020 Grid 2020). The cone indicates the dominant microbarom source direction at 2015 January 01 and 2015 July 01, respectively.

2DFD file that contains 30 frequency steps (0.0345–0.5476 Hz), which results in a soundscape reconstruction for propagating microbaroms ranging between 0.069–1.095 Hz. Based on the comparisons, it can be concluded that soundscapes give a good insight into the contribution of microbaroms within the infrasonic wavefield. Moreover, soundscapes can also be used for spectral analysis of the source regions. From the frequency analysis of both the soundscapes and observations, it follows that the microbarom signals are contained in a broad frequency range spanning from 0.1 to 0.5 Hz during the austral winter. Fig. 16 shows the central frequency content of the various microbarom source regions extracted from the soundscapes during one day of the austral summer and winter. The dominant microbarom source direction for the different periods (Fig. 6, 2015 January 01 and 2015 July 01) is highlighted as a cone, whereas the remaining source regions are made transparent. The initial microbarom source model of the soundscapes is based on Waxler *et al.* (2007), which account for the effects of bathymetry. Therefore, the bathymetry features (GEBCO 2020 Grid 2020) are highlighted within the figure by the grey contour lines. Spectral analyses of the microbarom source regions provide insights into the frequency signature of the global ambient noise field (Campus & Christie 2010; Marty 2019). The microbarom source peak is typically estimated to be at 0.2 Hz. However, within this study it has been shown that the microbarom frequency range is shifting seasonally. Knowing the frequency signature of the microbarom source regions enables to distinguish between different source regions, and specifically characterize and identify these. Implementing the operational 2DFD model of the ECMWF, with 36 frequency steps (0.0345–0.9695 Hz) and 36 directions, will provided additional insight into the higher frequency signature (0.069–1.939 Hz).

The climatology analysis has addressed the differences between soundscapes and observations, which is essential for future improvements of the detection algorithms and soundscape reconstructions. Moreover, the combination of observations and soundscapes may enhance the filtering of microbarom source contributions within the infrasonic wavefield. In conclusion, this new knowledge contributes to a better verification of the CTBT and better applicability of infrasound as a remote sensing technique for the upper atmosphere (Donn & Rind 1972; Smets 2018). The climatology analysis as performed within this paper can act as guidance. The analysis is modular and can be applied to any infrasound station or place on earth. Moreover, the analysis could play a role in the installation of future infrasound arrays. The soundscapes provide insights into the expected microbarom exposure at (future) infrasound arrays.

ACKNOWLEDGMENTS

All figures have been created using Generic Mapping Tools (Wessel *et al.* 2013). OdO and JA are funded by a Human Frontier Science Program Young Investigator Grant (SeabirdSound—RGY0072/2017). The contributions of PS and LE are funded through a VIDI project from the Netherlands Organisation for Scientific Research (NWO), project 864.14.005.

DATA AVAILABILITY

The authors thank the CTBTO and station operators for the high quality of IMS data and products, and the ECMWF ERA5 atmospheric re-analyses of the global climate. IMS data can be accessed through the vDEC (see https://www.ctbto.org/specials/vdec/). ERA5 can be accessed through the Copernicus Climate Change Service Climate Data Store (https://cds.climate.copernicus.eu/cdsapp#!/home).

REFERENCES

Alcoverro, B. & Le Pichon, A., 2005. Design and optimization of a noise reduction system for infrasonic measurements using elements with low acoustic impedance, *J. acoust. Soc. Am.,* **117**(4), 1717–1727.

Assink, J., Waxler, R. & Drob, D., 2012. On the sensitivity of infrasonic traveltimes in the equatorial region to the atmospheric tides, *J. geophys. Res.: Atmos.,* **117**(D1).

Assink, J., Waxler, R., Smets, P. & Evers, L., 2014. Bidirectional infrasonic ducts associated with sudden stratospheric warming events, *J. geophys. Res.: Atmos.,* **119**(3), 1140–1153.

Assink, J., Averbuch, G., Shani-Kadmiel, S., Smets, P. & Evers, L., 2018. A seismo-acoustic analysis of the 2017 North Korean nuclear test, *Seismol. Res. Lett.,* **89**(6), 2025–2033.

Assink, J., Smets, P., Marcillo, O., Weemstra, C., Lalande, J.-M., Waxler, R. & Evers, L., 2019. Advances in infrasonic remote sensing methods, in *Infrasound Monitoring for Atmospheric Studies,* pp. 605–632, Springer.

Bartlett, M., 1948. Smoothing periodograms from time-series with continuous spectra, *Nature,* **161**(4096), 686.

Blixt, E.M., Näsholm, S.P., Gibbons, S.J., Evers, L.G., Charlton-Perez, A.J., Orsolini, Y.J. & Kværna, T., 2019. Estimating tropospheric and stratospheric winds using infrasound from explosions, *J. acoust. Soc. Am.,* **146**(2), 973–982.

Bracewell, R.N., 1986. *The Fourier Transform and its Applications,* vol. **31999,** McGraw-Hill, New York.

Brachet, N., Brown, D., Le Bras, R., Cansi, Y., Mialle, P. & Coyne, J., 2010. Monitoring the earth?s atmosphere with the global ims infrasound network, in *Infrasound Monitoring for Atmospheric Atudies,* pp. 77–118, Springer.

Brekovskikh, L., 1973. Waves in layered media academic, new york, 1960, chap. 1. 31 ba auld, *Acoustic Fields and Waves in Solids*.

Brown, D., Ceranna, L., Prior, M., Mialle, P. & Le Bras, R.J., 2014. The idc seismic, hydroacoustic and infrasound global low and high noise models, *Pure appl. Geophys.,* **171**(3–5), 361–375.

Campus, P. & Christie, D., 2010. Worldwide observations of infrasonic waves, in *Infrasound Monitoring for Atmospheric Studies,* pp. 185–234, Springer.

Capon, J., 1969. High-resolution frequency-wavenumber spectrum analysis, *Proc. IEEE,* **57**(8), 1408–1418.

De Carlo, M., Ardhuin, F. & Le Pichon, A., 2020. Atmospheric infrasound generation by ocean waves in finite depth: unified theory and application to radiation patterns, *Geophys. J. Int.,* **221**(1), 569–585.

den Ouden, O.F.C., Assink, J.D., Smets, P.S., Shani-Kadmiel, S., Averbuch, G. & Evers, L.G., 2020. Clean beamforming for the enhanced detection of multiple infrasonic sources, *Geophys. J. Int.*

den Ouden, O.F.C., Smets, P.S., Assink, J.D. & Evers, L.G., 2021. A bird's-eye view on ambient infrasonic soundscapes, *Geophys. J. Int.,* **48,** e2021GL094555.

Donn, W. & Rind, D., 1972. Microbaroms and the temperature and wind of the upper atmosphere, *J. Atmos. Sci.,* **29**(1), 156–172.

Drob, D., 2019. Meteorology, climatology, and upper atmospheric composition for infrasound propagation modeling, in *Infrasound Monitoring for Atmospheric Studies,* pp. 485–508, Springer.

Drob, D.P., Picone, J. & Garcés, M., 2003. Global morphology of infrasound propagation, *J. geophys. Res.: Atmos.,* **108**(D21).

Era5, reanalysis., 2017. Boulder CO: Research Data Archive at the National Center for Atmospheric Research, Computational and Information Systems Laboratory. Retrieved from https://doi.org/10.5065/D6X34W69.

Evers, 2008. *The inaudible symphony: on the detection and source identification of atmospheric infrasound,* PhD thesis, TU Delft, Delft University of Technology.

Gabrielson, T.B., 2011. In situ calibration of atmospheric-infrasound sensors including the effects of wind-noise-reduction pipe systems, *J. acoust. Soc. Am.,* **130**(3), 1154–1163.

Gal, M., Reading, A., Ellingsen, S., Koper, K., Burlacu, R. & Gibbons, S., 2016. Deconvolution enhanced direction of arrival estimation using one-and three-component seismic arrays applied to ocean induced microseisms, *Geophys. J. Int.,* **206**(1), 345–359.

GEBCO 2020, Grid., 2020. GEBCO 2020 Grid, https://www.gebco.net/data_and_products/gridded_bathymetry_data/gebco_2020/.

Gossard, E.E. & Hooke, W.H., 1975. Waves in the atmosphere: atmospheric infrasound and gravity waves-their generation and propagation, *Atmos. Sci.,* **2,** Book: ISBN: 0444411968 9780444411969.

Green, D.N., 2015. The spatial coherence structure of infrasonic waves: analysis of data from international monitoring system arrays, *Geophys. J. Int.,* **201**(1), 377–389.

Haiden, T., Janousek, M., Bidlot, J., Buizza, R., Ferranti, L., Prates, F. & Vitart, F., 2018. *Evaluation of ECMWF Forecasts, including the 2018 Upgrade,* European Centre for Medium Range Weather Forecasts.

Hasselmann, K., 1963. A statistical analysis of the generation of microseisms, *Rev. Geophys.,* **1**(2), 177–210.

Högbom, J., 1974. Aperture synthesis with a non-regular distribution of interferometer baselines, *Astron. Astrophys. Suppl. Ser.,* **15,** 417.

Hupe, P., 2019. *Global infrasound observations and their relation to atmospheric tides and mountain waves,* PhD thesis, lmu.

Landes, M., Ceranna, L., Le Pichon, A. & Matoza, R.S., 2012. Localization of microbarom sources using the ims infrasound network, *J. geophys. Res.: Atmos.,* **117**(D6).

Le Pichon, A., Ceranna, L. & Vergoz, J., 2012. Incorporating numerical modeling into estimates of the detection capability of the ims infrasound network, *J. geophys. Res.: Atmos.,* **117**(D5).

Longuet-Higgins, M.S., 1950. A theory of the origin of microseisms, *Philos. Trans. R. Soc. Lond. A: Math. Phys. Eng. Sci.,* **243**(857), 1–35.

Marty, J., 2019. The ims infrasound network: current status and technological developments, in *Infrasound Monitoring for Atmospheric Studies,* pp. 3–62, Springer.

Matoza, R.S., Landès, M., Le Pichon, A., Ceranna, L. & Brown, D., 2013. Coherent ambient infrasound recorded by the international monitoring system, *Geophys. J. Int.,* **40**(2), 429–433.

McKee, K. *et al.*, 2021. Evaluating the state-of-the-art in remote volcanic eruption characterization part II: Ulawun volcano, papua new guinea, *J. Volc. Geotherm. Res.,* 107381.

Melton, B.S. & Bailey, L.F., 1957. Multiple signal correlators, *Geophysics,* **22**(3), 565–588.

Panel, D.B.C., 2005. Reference guide to the gts sub-system of the argos processing system. revision 1.6.

Raspet, R., Abbott, J.-P., Webster, J., Yu, J., Talmadge, C., Alberts, K. II, Collier, S. & Noble, J., 2019. New systems for wind noise reduction for infrasonic measurements, in *Infrasound Monitoring for Atmospheric Studies,* pp. 91–124, Springer.

Shumway, R.H., 1971. On detecting a signal in n stationarily correlated noise series, *Technometrics,* **13**(3), 499–519.

Šindelářová, T. *et al.*, 2021. Infrasound signature of the post-tropical storm ophelia at the central and eastern european infrasound network, *J. Atmos. Solar-Terrest. Phys.,* **217,** 105603.

Sleeman, R., Van Wettum, A. & Trampert, J., 2006. Three-channel correlation analysis: a new technique to measure instrumental noise of digitizers and seismic sensors, *Bull. seism. Soc. Am.,* **96**(1), 258–271.

Smets, 2018. Infrasound and the dynamical stratosphere: a new application for operational weather and climate prediction, *Delft Univ. Technol,* PhD Thesis: ISBN 978-94-6186-909-8.

Smets & Evers, 2014. The life cycle of a sudden stratospheric warming from infrasonic ambient noise observations, *J. geophys. Res.: Atmos.,* **119**(21), 12,084–12,099.

Stettner, F.B., 2018. *Infrasound data analysis of signals produced by Greenlandic glaciers,* Master's thesis, Utrecht University.

Sutherland, L.C. & Bass, H.E., 2004. Atmospheric absorption in the atmosphere up to 160 km, *J. acoust. Soc. Am.,* **115**(3), 1012–1032.

Szuberla, C.A., Olson, J.V. & Arnoult, K.M., 2009. Explosion localization via infrasound, *J. acoust. Soc. Am.,* **126**(5), EL112–EL116.

Tailpied, D., Pichon, A.L., Marchetti, E., Assink, J. & Vergniolle, S., 2016. Assessing and optimizing the performance of infrasound networks to monitor volcanic eruptions, *Geophys. J. Int.,* ggw400.

Viberg, M. & Krim, H., 1997. Two decades of array signal processing, in *Proc. 31st Asilomar Conf. Sig., Syst., Comput., Pacific Grove, CA*.

Vorobeva, E., De Carlo, M., Le Pichon, A., Espy, P.J. & Näsholm, S.P., 2020. Microbarom radiation and propagation model assessment using infrasound recordings: a vespagram-based approach, *Ann. Geophys. Discus.,* **2020,** 1–22.

Walker, K.T. & Hedlin, M.A., 2010. A review of wind-noise reduction methodologies, in *Infrasound Monitoring for Atmospheric Studies,* pp. 141–182, Springer.

Waxler, R. & Assink, J., 2019. Propagation modeling through realistic atmosphere and benchmarking, in *Infrasound Monitoring for Atmospheric Studies,* pp. 509–549, Springer.

Waxler, R. *et al.*, 2007. The effects of finite depth of the ocean on microbarom signals, in *8th International Conference on Theoretical and Computational Acoustics (ICTCA), Crete, Greece*.

Wessel, P., Smith, W.H., Scharroo, R., Luis, J. & Wobbe, F., 2013. Generic mapping tools: improved version released, *Eos, Trans. Am. geophys. Un.,* **94**(45), 409–410.

SUPPORTING INFORMATION

Supplementary data are available at *GJI* online.

R2_denOudenetal_GJI_SI.pdf

Please note: Oxford University Press is not responsible for the content or functionality of any supporting materials supplied by the authors. Any queries (other than missing material) should be directed to the corresponding author for the paper.